RMetS
Royal Meteorological Society

The role of heating and cooling associated with ice processes on tropical cyclogenesis and intensification

Gerard Kilroy,[a]* Roger K. Smith[a] and Michael T. Montgomery[b]

[a]*Meteorological Institute, Ludwig Maximilians University of Munich, Germany*
[b]*Department of Meteorology, Naval Postgraduate School, Monterey, CA, USA*

Correspondence to: G. Kilroy, Meteorological Institute, Ludwig-Maximilians University of Munich, Theresienstr. 37, 80333 Munich, Germany. E-mail: gerard.kilroy@lmu.de

A recent idealized numerical study of tropical cyclogenesis and subsequent intensification using warm-rain-only microphysics is extended to examine the modifications brought about by a representation of ice processes. It is found that the time taken to reach cyclogenesis is more than twice that in the equivalent warm-rain-only simulation. The subtle reasons for the difference in the length of the gestation period are discussed. A mid-level vortex forms during the early gestation period when ice processes are present, but not when warm-rain-only processes are present. Axisymmetric balance calculations show that the spin-up of this mid-level vortex is related to the different spatial distribution of diabatic heating rate in the presence of ice, which leads to a *system-scale* radial influx of absolute vorticity in the middle troposphere. The tropical-cyclone vortex that forms in the simulation with ice is similar to that in the warm-rain-only simulation, with the strengthening frictional boundary layer exerting a progressively important role in focusing inner-core deep convection. This vortex develops *in situ* on a much smaller scale than the mid-level vortex and there is no evidence that it is a result of the mid-level vortex being somehow carried downwards, as has been suggested previously by some researchers. Some implications of the results in relation to previous theories of tropical cyclogenesis are discussed.

1. Introduction

In a recent article, Kilroy *et al.* (2017, henceforth referred to as KSM) presented a series of idealized, convection-permitting numerical simulations of tropical cyclogenesis in a favourable, quiescent environment with a thermodynamic sounding based on data from an observed pre-genesis event. The calculations were initialized with a weak (maximum wind speed $5\,\mathrm{m\,s^{-1}}$), cloud-free, axisymmetric warm-cored vortex in thermal wind balance on an f-plane. It was shown that, during a gestation period on the order of two days, there is a progressive organization of convectively induced, cyclonic relative vorticity into a coherent monopole of cyclonic vorticity with a horizontal scale of approximately 25 km. This organization takes place at relatively low wind speeds, during a period in which there is only a small increase in the maximum azimuthally averaged wind speed. After this gestation period, the vortex intensifies rapidly, achieving hurricane strength within less than 12 h.

From an early stage, vortex evolution is well explained by the rotating convection paradigm for tropical cyclone intensification, articulated, for example, by Montgomery and Smith (2014, 2017a). The results of KSM provide strong support for the hypothesis of Montgomery and Smith (2011) that the genesis process is not fundamentally different from that of vortex intensification. Indeed, they indicate that the traditional approach of treating 'genesis' and 'intensification' as separate processes (e.g. Frank, 1987; Emanuel, 1989; McBride, 1995; Karyampudi and Pierce, 2002; Tory and Frank, 2010) is not necessary. In particular, KSM suggests that genesis does not require a 'trigger' and does not depend on the prior existence of a mid-level vortex.

A noteworthy idealization of the KSM study was the restriction to warm-rain-only processes in clouds, an idealization whose realism might be questioned. In the present article, this limitation is removed by repeating their control calculation with a representation of ice microphysical processes.

There have been many studies where ice microphysical processes have been included in tropical cyclone models. Two of the earliest we are aware of are those of Lord *et al.* (1984) and Willoughby *et al.* (1984), which both used the same axisymmetric, non-hydrostatic model. Lord *et al.* (1984) found, *inter alia*, that spin-up is delayed compared with an equivalent calculation with warm-rain-only microphysics, while Willoughby *et al.* (1984) found that rings of convection are much more common when ice is included. In an early numerical study of tropical convection with and without ice processes, McCumber *et al.* (1991) found that the inclusion of ice led to more realistic rainfall rates in the anvil region and to more realistic vertical cloud structure near the melting level.

An influential study of tropical cyclogenesis using a high-resolution three-dimensional model with ice processes included was that of Nolan (2007), the results of which were reviewed by KSM. One particularly noteworthy feature of Nolan's simulation, not captured by that of KSM, was the development first of a relatively strong mid-level vortex (maximum wind speed of $12 \, \text{m s}^{-1}$) prior to genesis. Since the occurrence of a mid-level vortex is a feature also of earlier genesis theories (e.g. Simpson *et al.*, 1997; Bister and Emanuel, 1998), one question might be whether such a vortex forms when ice microphysical processes are included in the KSM model and, if so, is this formation important in the genesis process?

The existence of a mid-level cyclonic vorticity maximum has been argued to be essential for tropical cyclogenesis by Raymond *et al.* (2011, 2014). If correct, this would imply that the marsupial paradigm of tropical cyclogenesis by Dunkerton *et al.* (2009), Montgomery *et al.* (2010) and Wang *et al.* (2010) is deficient in not accounting explicitly for the middle-level vortex in supporting the genesis process.

The Raymond *et al.* theory is derived from a numerical study using non-rotating, two-dimensional (slab-symmetric) radiative convective equilibrium simulations presented in Raymond and Sessions (2007). Those authors found that increased stabilization of the atmosphere, brought about by the generation of a warm temperature perturbation in the middle troposphere and a cold temperature perturbation in the lower troposphere, resulted in a concentrated inflow in a shallow layer in the lower troposphere. The proffered implication is that, if realistic values of ambient rotation associated with a tropical wave or monsoon trough were included, this convergence would import sufficient absolute vorticity to overcome that lost to the surface by friction. This thermodynamic control process is argued to be the critical ingredient in altering the vertical mass flux profile to lower the maximum mass flux and suppressing the lateral export of moist entropy (Raymond *et al.*, 2011, 2014). One of the advantages of the idealized configuration used in this study is that this theory can be tested with a fully three-dimensional model that includes rotational effects.

Early ideas on the importance of the middle-level cyclonic vortex in the cyclogenesis process included the viewpoint that the middle-level vortex descended to low levels, carrying the elevated cyclonic vorticity near to the surface and fostering frictional-based convergence and the organization of deep convection in a mesoscale region (e.g. Bister and Emanuel, 1998; Houze, 2004). Indeed, Houze (2004) writes: 'Tropical cyclones tend to spin up as the MCVs [mesoscale convective vortices: our insertion] of two or more MCSs [mesoscale convective systems: our insertion] rotate around a common centroid, which develops into the center of the cyclone. The mechanism by which the middle level cyclone congeals and builds downward toward the ocean surface is not clear'. Ten years later, in an exposition of clouds in the formative stages of hurricanes, Houze (2014) writes: 'As the larger depression gathers strength from all the ongoing convective activity and gradually takes on a tropical storm structure in its wind field, the probability increases that one of the MCSs with rotational convective cells and/or MCV will occur in the ideal spot (presumably the exact centre of the depression) where the MCS's cloud structure interacts with the vortex centre to metamorphose into a structure that has an incipient eye, eyewall, and rainbands'. The tentative nature of this explanation encapsulated in the idea of *a cloud structure interacting with the vortex centre* indicates that there remains a need to understand better how the low-level vortex forms.

Raymond and López-Carillo (2011) have pointed out that a net downward transport of cyclonic vertical vorticity across isobaric surfaces to the surface violates the theorem of Haynes and McIntyre (1987), which states that there can be no net transfer of absolute vertical vorticity across an isobaric surface. Nevertheless, the idea continues to be invoked as a pathway for the formation of a concentrated low-level vortex. The analysis of the present simulation enables one to revisit this topic and shed new light on the formation of the low-level vortex.

As far as we know, the only other idealized study of tropical cyclogenesis to carry out similar three-dimensional simulations with and without ice is that of Nicholls and Montgomery (2013). While they did show that genesis was delayed significantly in the presence of ice, they did not examine the reasons for this delay. The main focus of their work was on simulations including ice. They did find that a relatively strong mid-level vortex occurred in some, but not all, of their ice simulations and found two primary pathways in the cases with ice, with a strong dependence on the type of radiation scheme.

An idealized study of tropical cyclone intensification by Wang (2002) compared hydrostatic simulations with and without ice processes using his model TCM3. Starting with a moderately strong initial vortex (maximum tangential wind speed $20 \, \text{m s}^{-1}$), he found that 'although the cloud structures of the simulated tropical cyclone can be quite different with different cloud microphysics schemes, intensification rate and final intensity are not very sensitive to the details of the cloud microphysics parameterizations'. The warm-rain-only vortex was a little stronger and intensified a little sooner.

There have been a few case studies of tropical cyclogenesis and/or intensification in which the effects of ice microphysics have been investigated. For example, Zhu and Zhang (2006) compared simulations of Hurricane *Bonnie* (1998) with and without ice-microphysical processes. The simulated storm without ice was weaker than the four other simulations that included representations of ice. Zhu and Zhang attributed the weaker storm in the no-ice case to the lack of latent heat of fusion and neglect of the growth and rapid fallout of graupel.

Penny *et al.* (2016) analyzed numerical simulations of a non-developing disturbance using several different microphysics schemes, including one with warm-rain-only microphysics. While this simulation had the most rapid vortex development, it was not included in a detailed analysis comparing developing and non-developing vortices.

The purpose of this article is not to examine the role of ice microphysics *per se* by comparing simulations with different representations of ice microphysical processes as in some of the above studies, but rather to investigate the differences between simulations with and without a particular representation of ice microphysics (sections 3, 4 and 5). One aim is to examine whether a mid-level vortex forms when ice processes are included and to understand the additional effects of ice processes within the context of the rotating-convection paradigm for intensification. Another aim is to examine whether the unified view of tropical cyclogenesis and intensification in a favourable environment suggested by the warm-rain simulations of KSM extends also to the case with ice.

2. The numerical model and experimental design

The control simulation described and analyzed herein (referred to simply as Ex-I) has the same configuration as the warm-rain control simulation (referred to hereafter as Ex-WR) described in KSM. It is carried out also using the numerical model CM1 version 16, a non-hydrostatic and fully compressible cloud model (Bryan and Fritsch, 2002). In brief, the domain is $3000 \times 3000 \, \text{km}^2$ in size, with variable grid spacing reaching 10 km near the domain boundaries. The inner $300 \times 300 \, \text{km}^2$ has a 500 m grid spacing. The domain has 40 vertical levels, beginning at a height of 25 m and extending to a height of 25 km. The vertical grid spacing expands gradually from 50 m near the surface to 1200 m at the top of the domain. The Coriolis parameter $f = 2.53 \times 10^{-5} \, \text{s}^{-1}$, corresponding to $10°\text{N}$. The maximum tangential wind speed of the initial vortex ($5 \, \text{m s}^{-1}$) occurs at the surface at a radius of 100 km. The only differences from the KSM simulation are the inclusion of ice microphysical processes using the Morrison
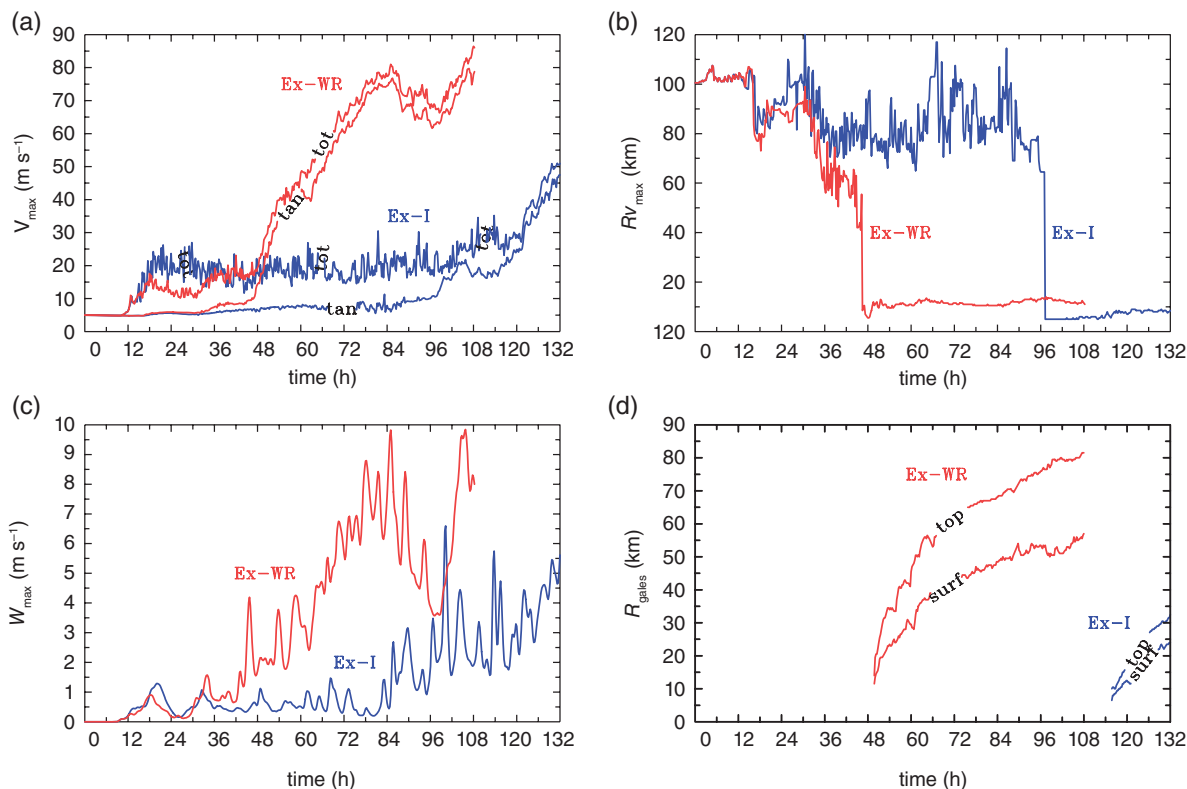
Figure 1. Time series for both Ex-I and Ex-WR of (a) maximum total wind speed (VT_{max}, curve labelled 'tot') and maximum azimuthally averaged tangential wind speed (V_{max}, curve labelled 'tan'). Panel (b) shows the radius $R_{v\,max}$ at which V_{max} occurs. Panel (c) shows the smoothed azimuthally averaged maximum vertical velocity. Panel (d) shows the radius at which gale force winds occur (R_{gales}), where R_{gales} is calculated at a height of 1 km (labelled 'top') and corresponds to the radius of 17 m s^{-1} tangential winds outside the eyewall. Also shown is the radius at which gale force winds occur calculated at the surface (labelled 'surf'), corresponding to the radius of 17 m s^{-1} total wind speed outside the eyewall. [Colour figure can be viewed at wileyonlinelibrary.com].

double-moment ice microphysical scheme* (Morrison *et al.*, 2005) and the longer integration time (132 h instead of 108 h), because of the longer time required for the vortex to intensify. The reference sounding is described in KSM (see their figure 1). In brief, it is an arithmetic mean of 39 dropsonde soundings obtained on 12 September 2010, during the Pre-Depression Investigation of Cloud Systems in the Tropics (PREDICT) field campaign (Smith and Montgomery, 2012). This sounding has a Convective Available Potential Energy (CAPE) of 2028 J kg^{-1}, a Convection Inhibition (CIN)† of 47 J kg^{-1} and a Total Precipitable Water (TPW) of 61 kg m^{-2}. The sea-surface temperature is 29 °C, typical of the Caribbean region at the time of the PREDICT experiment.

As in KSM, we perform two additional simulations with random moisture perturbations of up to 0.5 g kg^{-1} applied from the surface to a height of 1 km. The purpose of these experiments, referred to as 'P1' and 'P2', respectively, is to add robustness to the results by taking into consideration the stochastic nature of deep convection. The results of these simulations are discussed in section 6.

3. Vortex evolution with and without ice

Figure 1 compares the evolution of azimuthally averaged quantities in the two simulations Ex-I and Ex-WR, including the maximum tangential wind speed (V_{max}), the radius at which this maximum occurs ($R_{v\,max}$), the smoothed (1−2−1 filter in time, used five times) maximum vertical velocity (W_{max}), the radius of total gale force winds (17 m s^{-1}) at the surface (R_{galesF}, labelled 'surf') and the radius of the gale-force tangential wind component at a height of 1 km (R_{gales}, labelled 'top'). Also shown is the maximum total horizontal wind speed, VT_{max}.

For the first 45 h of the simulation, the V_{max} time series for the two simulations remain close to each other. Thereafter, the vortex in Ex-WR begins to intensify rapidly. As shown and explained in KSM, VT_{max} increases before V_{max}, as it incorporates localized wind-speed fluctuations associated with deep convection that do not project significantly on to the azimuthal average. In Ex-I, VT_{max} begins to exceed V_{max} at about the same time as in Ex-WR, indicating that deep convection begins to occur at about the same time in both experiments (see later). However, the V_{max} and corresponding VT_{max} curves are further apart for a longer period of time than in Ex-WR, a reflection of the fact that wind-speed fluctuations associated with deep convection are larger when ice microphysical processes are included. The gestation period in Ex-I is more than double that of Ex-WR.

While the point of rapid intensification (referred to by KSM as the intensification begin time) is rather easily identified in Ex-WR, it is less clear in Ex-I, at least without an investigation of other metrics. On the basis of V_{max}, one might judge it to be at either 100 h or 115 h. In this simulation, V_{max} increases steadily from 5 to 10 m s^{-1} in the first 95 h, while from 95 to 132 h it increases to almost 50 m s^{-1}. Note that the intensification rate in Ex-I is barely half that in Ex-WR.

In both simulations, $R_{v\,max}$ begins to fluctuate as deep convection starts to occur, presumably as a result of radial wind fluctuations generated by the convection, which in an aggregate sense would advect the absolute angular momentum surfaces (*M*-surfaces) inwards or outwards. $R_{v\,max}$ shows a sharp decline at about 46 h in Ex-WR and at about 97 h in Ex-I, in both cases signifying the formation of a narrow vortex core at the respective times. Subsequently, this inner vortex has a time-mean $R_{v\,max}$ of about 7 km in Ex-I, compared with approximately 11 km in Ex-WR. While these radii are small, they are within the range of values observed. For example, values of $R_{v\,max}$ in Australian region Tropical Cyclones *Ada* (1970), *Tracy* (1974) and *Kathy* (1984) were 9, 7 and 10 km, respectively (Callaghan and Smith, 1998) and those in Atlantic Hurricanes *Allen* (1980), *Charley*

---

*In KSM, the Kessler warm-rain scheme is employed.
†The method used to calculate CAPE and CIN is the same as that described in the appendix of Smith and Montgomery (2012).

(2004) and *Ivan* (2004) were 10, 13 and 9 km, respectively (Lajoie and Walsh, 2008). In idealized numerical simulations, the mature inner-core size of the simulated storm is related, *inter alia*, to the initial vortex size (Kilroy and Smith, 2017).

Significantly, the W_{max} time series are similar for both simulations until about 18 h, whereafter there is a short period (on the order of a few hours) when W_{max} is slightly larger in Ex-I. At about 25 h, W_{max} has fallen to almost zero in both experiments, a reflection of the temporary decline in deep convective activity. As deep convection redevelops, the time series for Ex-WR shows a prolonged increase (with fluctuations) from about 30 h to about 85 h. In Ex-I, the prolonged increase begins first after 80 h and continues until the end of the calculation.

Coincidentally,[‡] in Ex-WR, both R_{gales} and R_{galesF} appear first at about 50 h. Thereafter, both increase steadily, with R_{gales} exceeding R_{galesF}. In contrast, in Ex-I, gales occur only after about 115 h.

In the next three subsections, we consider the differences in evolution between the two control experiments. To begin with, in section 3.1 we examine the differences when the first bout of convection forms. Then, in section 3.2, we examine the differences in the early evolution up to the time at which rapid intensification occurs in Ex-WR. Finally, in section 3.3, we explain why intensification is delayed at later times when ice microphysics is included. A brief summary of the differences is presented in section 3.4.

3.1. Similarity of warm rain and rain + ice simulations

There is one issue that needs to be investigated first when comparing the two simulations with and without a representation of ice microphysics. As found by Kilroy *et al.* (2014) for the case of a single convective cell initiated by a prescribed thermal perturbation, there can be differences in the formulation of the warm-rain component of an ice microphysics scheme and the Kessler warm-rain scheme (see the footnote in Kilroy *et al.* (2014, p1765)). For example, when using the Gilmore ice scheme, Kilroy *et al.* found that the maximum vertical velocity at an altitude on 2 km was of the order of 20% larger when ice processes were included, although at that stage no ice had formed at this altitude! One could anticipate similar differences in updraught strength between the Morrison scheme used in Ex-I and the Kessler scheme used in Ex-WR. However, the close similarity between the W_{max} time series in Ex-I and Ex-WR suggests that the differences in this case may not be significant.

To examine the foregoing issue further, in Figure 2 we compare horizontal cross-sections of the difference in water-vapour mixing ratio from its initial value at a height of 1 km in Ex-I and Ex-WR at 10 h intervals up to 30 h. Each panel includes horizontal wind vectors to show the circulation and three contours of vertical velocity: one showing upward motion at a height of 3 km to indicate the location of convective updraughts (at 10 h the convection is not yet deep), another showing subsidence at a height of 1 km and one showing the zero contour. Notably, at 10 h (panels (a) and (b)) all fields are identical, as is W_{max} in Figure 1 (the W_{max} curves in both experiments remain identical until about 12 h). At this time (10 h), there are no perturbations of water-vapour mixing ratio at a height of 6 km (just above the freezing level), indicating that ice has not yet formed (not shown). These results indicate that the Kessler warm-rain scheme and the warm-rain component in the Morrison scheme are sufficiently similar to make comparisons between the two simulations meaningful.

3.2. Interpretation of early differences with and without ice

The reasons for delayed vortex intensification in Ex-I are subtle. As the flows in the two simulations Ex-I and Ex-WR continue

to evolve following the onset of deep convection, the patterns of water-vapour mixing ratio at a height of 1 km shown in Figure 2 begin to differ. At 20 h and beyond, the patterns of convective updraughts at a height of 3 km in the two simulations are completely different. While the inner-core region of the vortex in Ex-WR becomes progressively moister (Figures 2(d) and (f)), that in Ex-I becomes progressively drier (Figures 2(c) and (e)).

As a first step to pinpoint the reasons for the foregoing differences in evolution, in Figure 3 we show the early evolution (up to 24 h) of W_{max} together with smoothed time series of maximum local vertical velocity WT_{max}, the smoothed height at which WT_{max} occurs, $Z_{WT_{max}}$, and the smoothed minimum local vertical velocity WT_{min} in both simulations. The time smoothing is accomplished by applying a $1-2-1$ filter five times. It is seen that there is stronger vertical motion in Ex-I, even in an azimuthally averaged sense, with W_{max} larger from $12-16$ h and from 18 h onwards than in Ex-WR. It is reasonable to surmise that this mostly larger W_{max} is due to the additional latent heat release associated with the formation of ice hydrometeors. Indeed, Figures 3(b) and (d) show that, at most times from about 12 h when ice first forms, WT_{max} and WT_{min} are largest in magnitude in Ex-I and the height of WT_{max} is largest also. The inference from Figure 3 is that both convective updraughts and downdraughts tend to be stronger in the presence of ice, consistent with estimates from parcel calculations when the latent heat of freezing is included (see e.g. Williams and Renno, 1993; Zipser, 2003).

A possible explanation for the inner-core drying at 1 km in Ex-I could be the geometric effect of stronger deep convection in Ex-I forcing a region of mesoscale subsidence about the circulation axis, which would bring drier air to low levels. Strictly, the geometric argument would assume that the convection in the two simulations remains broadly at the same radii. While this is true at 10 h, it becomes progressively less true at later times. Nevertheless, the region of drying in Ex-I seen in Figure 2(c) and (e) does coincide with a broad region of weak subsidence at both 20 and 30 h.

Figure 4 shows the time–height cross-sections of vertical mass flux averaged over a square column of cross-sectional area $20 \times 20 \, km^2$ and $60 \times 60 \, km^2$, centred on the domain centre. In the $20 \times 20 \, km^2$ column, there is stronger subsidence below 4 km height in Ex-I during the times shown. In Ex-WR there is predominantly upward mass flux beyond about 20 h, while in Ex-I there are periods of alternating upward and downward mass flux during the first 24 h. Since deep convection remains outside the $20 \times 20 \, km^2$ column during the first 20 h in Ex-I (see top and middle panels of Figure 2), the subsidence in the inner core cannot be associated with convective downdraughts. It must be forced subsidence associated with the convection at larger radii.

In the $60 \times 60 \, km^2$ column, there are small differences between the vertical mass flux in the two simulations at early times. In Ex-WR, the mass flux profile in this column becomes positive after about 17 h, whereas there are periods of net downward motion in Ex-I until 21 h.

In summary, in both averaging columns, there is stronger net subsidence in Ex-I immediately after the first bout of deep convection, especially in the inner core region. This subsidence and the accompanying drying would act to impede the development of further deep convection in the inner core. In Ex-WR, the drying is weaker and deep convection begins to occur within 20 km of the circulation centre as early as 20 h (Figure 4(b)).

To understand fully why convection does not occur near the circulation centre in Ex-I, it is pertinent to examine how the average inner-core thermodynamic sounding evolves in both experiments at early times and what role the drying plays in Ex-I. Figure 5 shows the evolution of the CAPE and CIN for both simulations. These quantities are calculated from a thermodynamic sounding averaged over a $20 \times 20 \, km^2$ column centred on the circulation centre. Until 18 h, the evolution of CAPE and CIN in the inner core is essentially the same in

---

[‡]Recall that the definition of R_{galesF} is based on the total near-surface wind speed, whereas R_{gales} is based on the tangential wind component only.
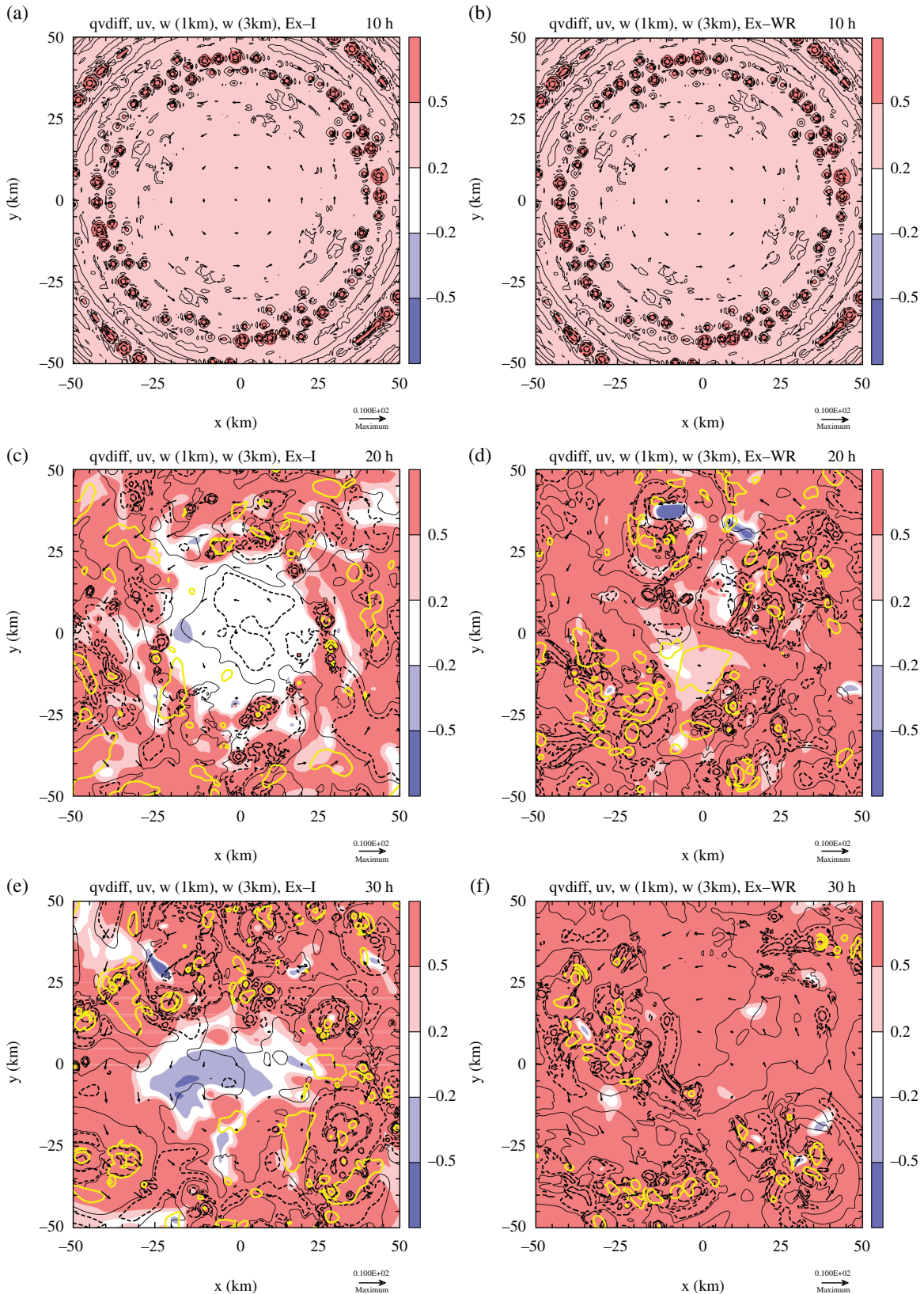
Figure 2. Horizontal cross-sections of water-vapour mixing ratio difference from the initial time at a height of 1 km in (a, c, e) Ex-I and (b, d, f) Ex-WR, at 10 h intervals from 10–30 h. Also shown are three contours of vertical velocity (ascent at a height of 3 km, contour 0.2 m s^{-1} (solid yellow contour), subsidence at a height of 1 km, contour −0.1 m s^{-1} (black dashed contour) and zero motion (thin solid black contour)) and horizontal wind vectors at a height of 1 km. Values for the shading of water-vapour mixing ratio difference are given in the colour bar, in units of g kg^{-1}. The wind vectors are in relation to the maximum reference vector (10 m s^{-1}) at the bottom right of each panel.

both experiments. In Ex-WR there is a sharp increase in CAPE and a decrease in CIN around 18 h, a change that is presumably associated with inner-core moistening. The subsequent reduction of CAPE at about 20 h is associated with deep convective cells forming in this inner core and consuming the CAPE.

In Ex-I, the stronger inner-core subsidence and subsequent mid-level drying keep the CIN relatively high for longer, although

the CAPE builds up gradually due to surface latent heat fluxes. Even with high CAPE, which remains large until about 60 h (Figure 5(b)), the relatively large CIN prevents deep convective cells from forming near the circulation centre.

Based on Figures 2–5, a schematic of the foregoing differences in early evolution between Ex-WR and Ex-I is shown in Figure 6. In essence, the vortex evolution in the two simulations is the
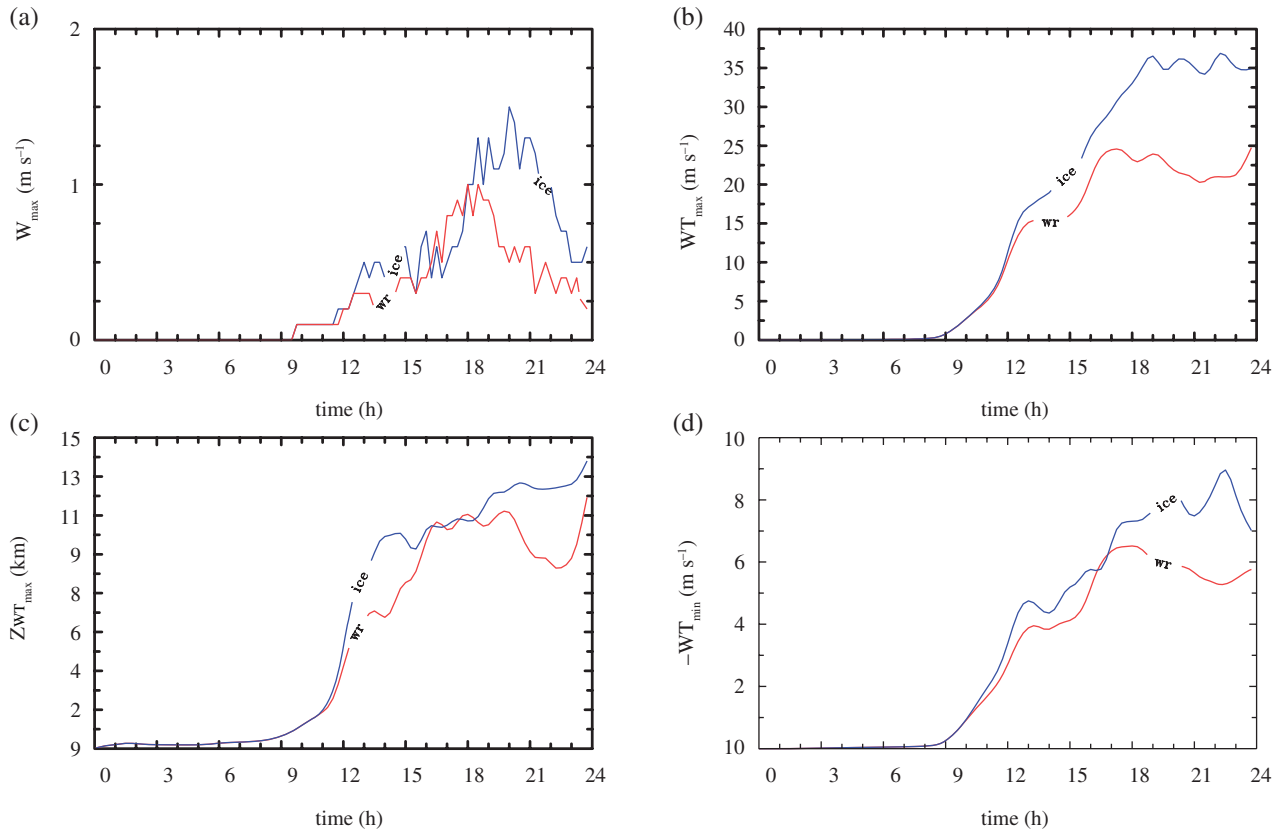
Figure 3. (a) Time series of maximum azimuthally averaged vertical wind speed (W_{max}) for the first 24 h in both experiments. Panel (b) shows the time-smoothed total maximum vertical velocity (WT_{max}) for the first 24 h, while panel (c) shows the height of this maximum. Panel (d) shows the time-smoothed total minimum vertical velocity ($-WT_{min}$) for the first 24 h. Ex-I is labelled 'ice' and Ex-WR is labelled 'wr'. The time smoothing is accomplished by applying a $1-2-1$ filter five times. [Colour figure can be viewed at wileyonlinelibrary.com].
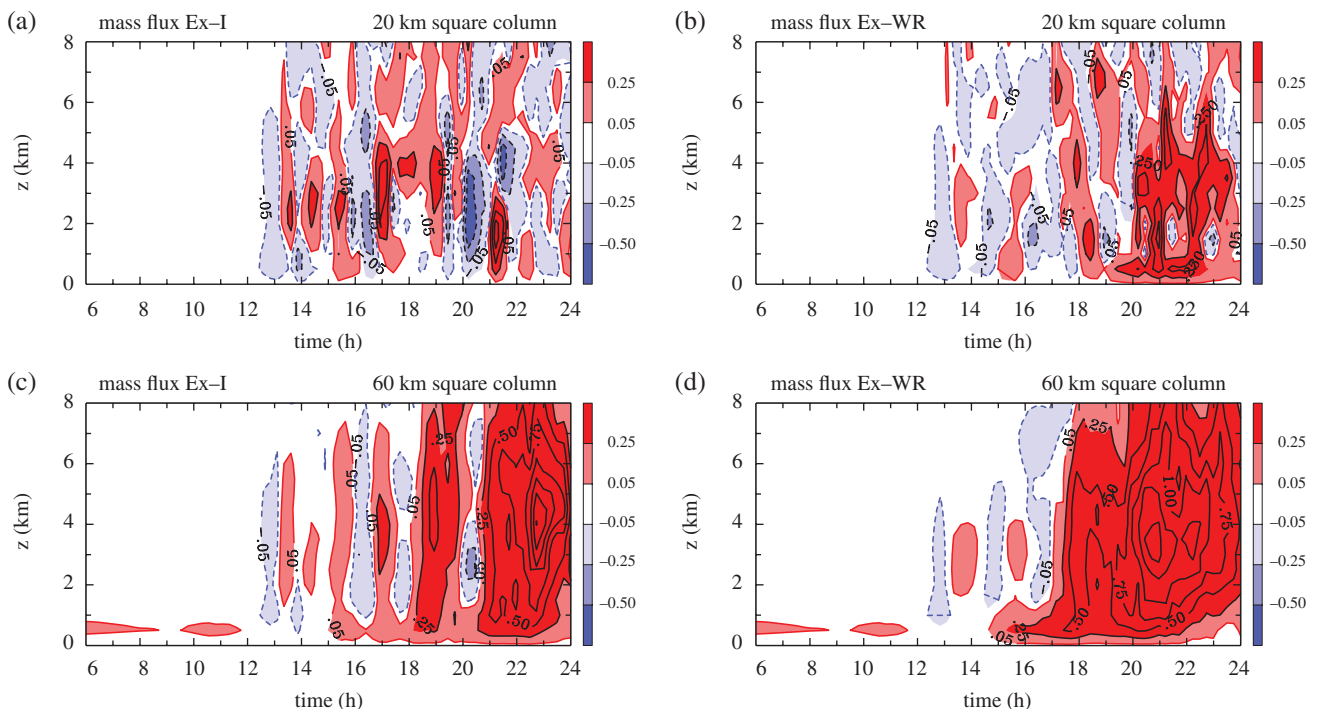
Figure 4. Time−height cross-sections of system-averaged vertical mass flux within (a, b) a 20 km ×20 km column and (c, d) a 60 km ×60 km column, centred on the domain centre for the first 24 h of the simulation. Ex-I is shown on the left, Ex-WR on the right. Values for the shading of mass flux are given in the colour bar, in units of kg m^{-2} s^{-1} multiplied by 10 for plotting purposes. Thick black contours are used for values every 0.25 kg m^{-2} s^{-1} from ±0.25 kg m^{-2} s^{-1}. Solid contours are positive, dashed contours negative.

same until ice hydrometeors form at around 12 h. The additional latent heat released by the formation of ice in Ex-I leads, *inter alia*, to stronger convective updraughts. At early times, before deep convection has formed in the inner core region, the subsidence there forced by deep convection at larger radii is stronger and deeper in Ex-I than in Ex-WR. At least when the deep convection

in the two experiments is located at similar radii to those in Figures 2(a) and (b), the stronger and deeper subsidence at lesser radii forced by this convection leads to a greater warming and drying there, preventing the development of deep convection in that region. In Ex-WR, the drying and warming is sufficiently weak to allow deep convection to develop near the circulation
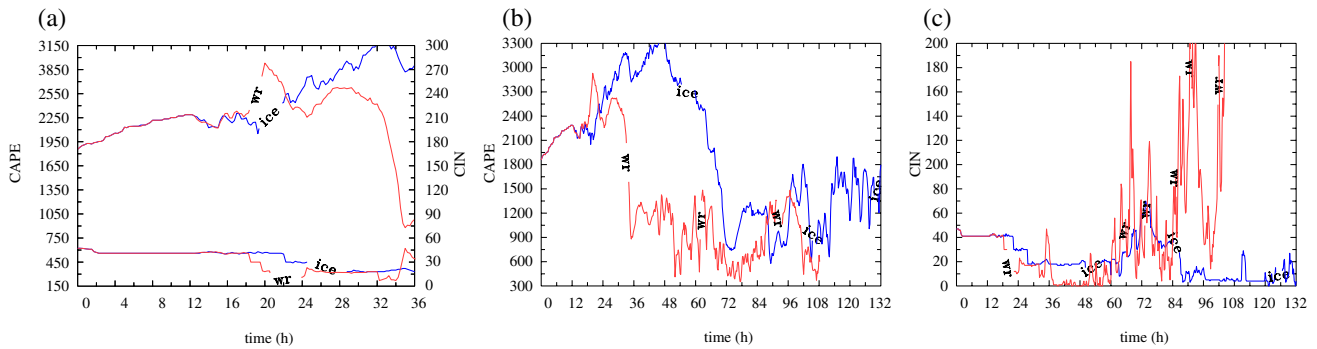
Figure 5. Evolution of CAPE and CIN, calculated from a sounding of an inner core average 20 km ×20 km column: (a) CAPE and CIN at early times out to 36 h, (b) CAPE out to 132 h and (c) CIN out to 132 h for both experiments. Ex-I is labelled 'ice' and Ex-WR is labelled 'wr'. Blue curves are for Ex-I and red curves for Ex-WR. The units of the displayed CAPE and CIN are J kg^{-1}. [Colour figure can be viewed at wileyonlinelibrary.com].

centre within 24 h of the simulation. This development of deep convection leads to a moistening at these inner radii and thereby to a reduction of the CIN. Although the CAPE builds up at these radii in both simulations, the stronger warming and drying in Ex-I is sufficient to keep the CIN high enough near the circulation centre to inhibit deep convection forming.

Several recent studies (e.g. Smith *et al.*, 2015a; Kilroy *et al.*, 2016a; Tang *et al.*, 2016) have highlighted the importance, in general, of sustained deep convection occurring close to the centre of an existing circulation for vortex intensification. The reason is that convection in such a location is most effective in converging absolute angular momentum above the frictional boundary layer, where this quantity is approximately materially conserved, resulting in spin-up of the tangential winds (see e.g. Smith and Montgomery, 2016a, section 3.2).§ One key requirement for sustained deep convection to occur near the circulation centre is the presence of low CIN there. Another requirement is that any convection that forms has low propensity to produce strong convective downdraughts that might otherwise flood the boundary layer with air having relatively low θ_e.

In the next section, we examine the evolution beyond the initial 30 h, seeking to understand why intensification is delayed until 90 h in Ex-I.

3.3. Why does ice delay intensification further?

In the previous section, we examined the early differences between the two simulations and explained why deep convection does not occur in the inner core in Ex-I within the first 24 h of the simulation. However, in Ex-I, V_{max} does not increase appreciably for a further 66 h (i.e. until after 90 h: see Figure 1(a)), about the same time as the first significant increase in W_{max}. Soon after (at about 97 h), the radius of maximum winds decreases to near 7 km. In this section, we offer an explanation for why it takes so much longer for genesis to occur in Ex-I than in Ex-WR.

In Ex-WR, the intensification begin time, as defined in KSM, is at 45 h, although convection begins to flare continuously near the circulation centre as early as 30 h (see, for example, figure 8(e) of KSM). As long as the CIN remains low, deep convection can continue to occur near the circulation centre and can continue to draw absolute angular momentum surfaces inwards in the lower troposphere. Referring again to Figure 5, the CAPE in Ex-WR

increases gradually to 30 h as the boundary layer moistens. Shortly afterwards it falls dramatically, possibly suggesting that deep convection has developed near the circulation centre, consuming much of the CAPE that had been built up. That this does indeed happen is confirmed in animations of the vertical velocity field (not shown). The CIN falls to near-zero around this time also. In the subsequent 12 h of the simulation, the system undergoes a rapid intensification phase. In Ex-I, however, a dramatic depletion of CAPE in the inner core (between 60 and 72 h) coincides with a significant increase in CIN (to about 70 J kg^{-1} at 72 h). This large increase in CIN prolongs the genesis time in Ex-I and the next question is: why does this increase occur?

Based on results of Srivastava (1987), who showed that convective downdraughts are stronger with the inclusion of ice microphysics, Simpson *et al.* (1997) and Montgomery *et al.* (2010) suggested that the effect of stronger downdraughts would lead to a greater flooding of the boundary layer with air with relatively low equivalent potential temperature, a process that would delay vortex development. The effect of downdraughts reducing the boundary layer θ_e was discussed earlier by Barnes *et al.* (1983). Following these ideas, to investigate why the CIN increases markedly around 72 h in Ex-I, in Figure 7 we show horizontal cross-sections of the near-surface (at a height of 25 m) θ_e difference (shading) from its far-field value in Ex-I at 60 and 72 h. These times correspond with periods of high inner-core CAPE (panel (a)) and periods where CAPE is rapidly being consumed and CIN is increasing (panel (b)). Shown also are wind vectors at a height of 1 km. At 60 h, there is a broadly positive θ_e difference in the inner core region, while there are a few patches of reduced θ_e due to convective downdraughts, for example centred at $(-29$ km, -50 km), $(-47$ km, -23 km) and $(37$ km, 20 km). At 72 h, when the CAPE in the inner core of Ex-I is close to its lowest value for the 108 h shown, the circulation centre is engulfed by low θ_e. There follows a recovery period in the inner core lasting approximately 8 h, where essentially no deep convection occurs until the θ_e differences become positive again (not shown).

Until the intensification begin time ($\sim$100 or 115 h), there are alternate periods of sporadic convective activity in the inner core, with a subsequent lowering of low-level θ_e, followed by intervals of boundary-layer recovery.

The recovery period following the bout of convection at 72 h described above coincides with a period of little to no convective activity that lasts until about 80 h (Figure 1(c)). To illustrate this behaviour, in Figure 8 we show horizontal cross-sections of vertical vorticity, wind vectors at a height of 1 km and surface pressure at 10 h intervals from 80–110 h. Contours of vertical velocity equal to 1 m s^{-1} at heights of 2 and 6 km are superimposed to indicate the location of strong updraughts at these levels. At 80 h, the centre of circulation, as indicated by the velocity vectors, lies near the centre of the computational grid. At this time (80 h) there are no convective cells stronger than 1 m s^{-1} at heights of 2 or 6 km, indicating that there is no deep convection occurring at this time. Notably, there are hardly any patches of enhanced vertical vorticity exceeding 1×10^{-3} s^{-1}.

§Many earlier studies (see for example Vigh and Schubert (2009) and references therein) have proposed an alternative explanation, based on the idea that deep convection in the inertially stable inner core region is in some sense 'more efficient' than that at larger radii. The explanation is based on the idea that, if a specified diabatic heating distribution is located in a region with high inertial stability, it will induce a weaker updraught (inhibited by the larger resistance to radial motion) than if it were located in a region of weak inertial stability. The weaker updraught will be accompanied by less adiabatic cooling, thereby leading to a larger net heating of the updraught. The validity of this idea is questioned by Smith and Montgomery (2016a), who pointed out that, in reality, a weaker updraught would imply a reduced diabatic heating rate.
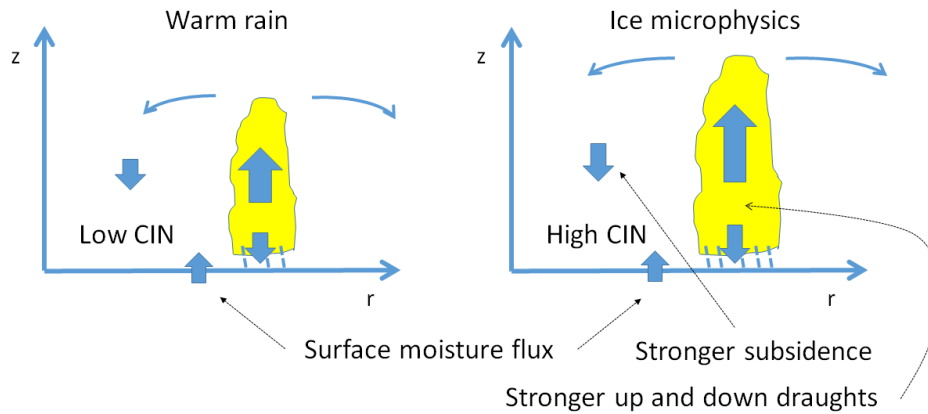
Figure 6. Schematic portraying the subtle differences between the genesis process in simulations Ex-WR and Ex-I. In each case, early deep convection develops away from the axis of the initial weak vortex. The collective effect of this convection, shown schematically as a single cloud in the figure, is to drive an overturning circulation with subsidence inside and outside the convective region. The release of latent heat of freezing in the Ex-I simulation leads to stronger convection and hence a stronger overturning circulation with stronger subsidence. The stronger subsidence radially inside the convection in this case leads to increased CIN that tends to inhibit the development of deep convection in this region. The stronger downdraughts in this case tend to flood the boundary layer with low θ_e air, again delaying the formation of deep convection near the centre of circulation. [Colour figure can be viewed at wileyonlinelibrary.com].
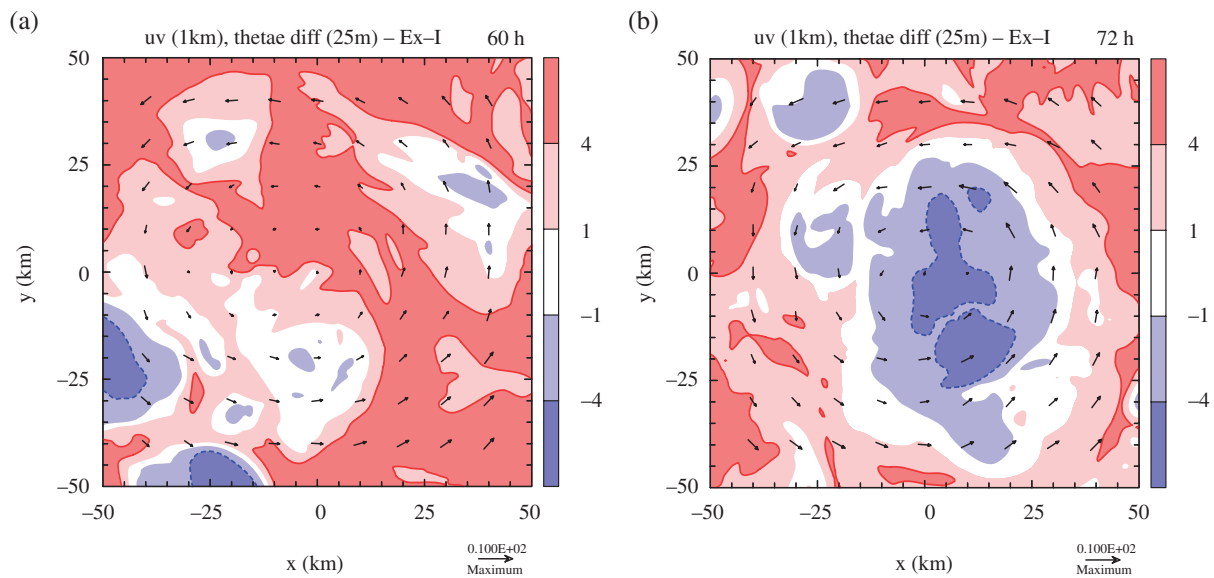
Figure 7. Horizontal cross-sections of θ_e difference from its initial value in Ex-I at (a) 60 and (b) 72 h. Also shown are horizontal wind vectors at a height of 1 km. Values for the shading of θ_e difference are given in the colour bar, in units of K. The wind vectors are in relation to the maximum reference vector ($10\,\mathrm{m\,s^{-1}}$) at the bottom right of each panel. The dashed contour highlights values of θ_e difference greater than -4 K.

After the inner core θ_e has recovered and the CIN has reduced to a value close to zero (Figure 5), deep convection is able to resume in the inner core. At 90 h (Figure 8(b)), there is a dramatic change in the vertical velocity and vertical vorticity fields near the circulation centre from 10 h earlier, with a monopole of cyclonic vertical vorticity present in the inner core and active deep convection co-located over the monopole. There is what appears to be a spiral rain-band feature also, with active deep convection and vorticity dipoles extending out from the circulation centre. These vorticity dipoles are the result of the tilting of background horizontal vorticity into the vertical. At 100 h the rainband has all but decayed, although there remains a core of strong vertical vorticity at the circulation centre. There is now persistent deep convection over the vorticity monopole, which stretches the cyclonic vorticity there further. At this time there is a lowering of the surface pressure in the vortex centre, as indicated by the presence of black contours.

At around 100 h, the cycle of deep convection and recovery ends and deep convection becomes continuous (subsequently w_{max} increases in strength around these times; see Figure 1(c)). At 110 h, there are significant differences evident in vortex structure from 10 h earlier. While the central pressure has not fallen further, deep convection has become widespread. There are patches also

of cyclonic vorticity just outside the inner-core monopole that appear to be wrapping around the monopole. After this time, V_{max} and VT_{max} begin to increase considerably in strength (see Figure 1(a)).

3.4. Summary

Summarizing the results of sections 3.2 and 3.3, the reduction of inner-core CIN in the Ex-WR simulation allows bouts of convection to occur near to the circulation centre after about a day. This reduction of CIN results predominantly from enhanced surface moisture fluxes, but is opposed to a degree by inner-core subsidence induced by convection at larger radii. In contrast, in the Ex-I simulation, at early times the induced subsidence is stronger because deep convection at larger radii is stronger. As a result, the inner core region becomes drier and has higher CIN than in the Ex-WR simulation. When deep convection does occur in the inner core region in the Ex-I simulation, the strong downdraughts associated with ice processes flood the boundary layer with low θ_e air, which is detrimental to the persistence of convection.

As time proceeds, this low θ_e air is steadily modified, predominantly by the persistent surface moisture fluxes, allowing
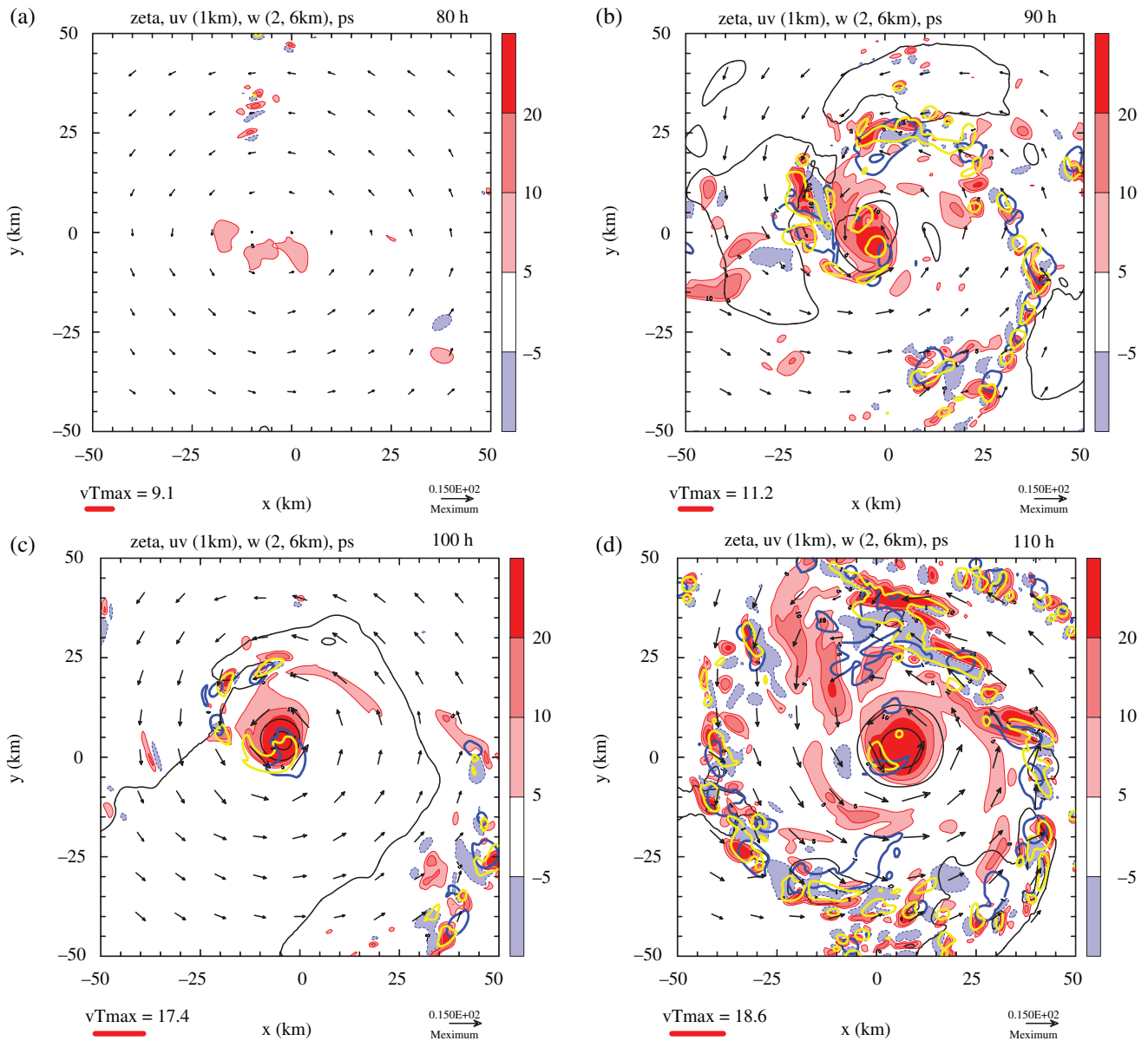
Figure 8. Horizontal cross-sections of relative vertical vorticity and wind vector at (a) 80, (b) 90, (c) 100 and (d) 110 h at 1 km altitude for Ex-I. Also shown are contours of vertical velocity at heights of 2 km (aqua) and 6 km (yellow) and black contours of surface pressure, contoured every 2 hPa. Values for the shading of vertical vorticity are given in the colour bar, multiplied by 10^{-4}. The vertical velocity contour is $1\,\mathrm{m\,s^{-1}}$ for both heights. The wind vectors are in relation to the maximum reference vector ($15\,\mathrm{m\,s^{-1}}$) at the bottom right of each panel, while at the bottom left the maximum total wind speed in the domain plotted is given in $\mathrm{m\,s^{-1}}$.

subsequent bouts of convection to occur. Successive bouts of deep convection serve to moisten the middle troposphere in the inner core and eventually deep convection becomes persistent near the circulation centre.

4. An azimuthally averaged view of vortex evolution

While the features of the genesis process described above are intrinsically asymmetric, it is insightful to consider an azimuthally averaged view of the process. To this end, Figure 9 shows vertical cross-sections of various azimuthally averaged and 3 h time-averaged quantities in the Ex-I simulation at 24 h intervals to 120 h, roughly spanning the gestation period prior to genesis. For comparison, Figure 10 shows similar plots for the Ex-WR simulation, but at 12 h intervals from 24−60 h, again approximately spanning the gestation period in this case. The time averaging is based on 15 min model output centred on the time indicated. The quantities shown are tangential, $\langle v(r,z)\rangle$, radial, $\langle u(r,z)\rangle$, and vertical, $\langle w(r,z)\rangle$, velocity components, the diabatic heating rate, $\langle \dot{\theta}(r,z)\rangle$, and the contours of absolute angular momentum $\langle M(r,z)\rangle$ (here we use angle brackets $\langle\rangle$ to denote an azimuthal average quantity). The vertical velocity and

diabatic heating rate provide a perspective on the evolution of the convectively induced secondary circulation in relation to features in the horizontal flow field.

Even though the time series in Figure 1(a) indicates little change in $V_{\max}$ before about 100 h in the Ex-I simulation, there are considerable changes in the structure of $\langle v(r,z)\rangle$ during this time. In particular, in contrast to the vortex in the Ex-WR simulation, the strongest tangential winds develop first at middle tropospheric levels rather than at low levels (e.g. Figures 9(a), (c) and (e)) and by 120 h there is a band of moderately strong ($> 10\,\mathrm{m\,s^{-1}}$) tangential winds at mid-levels extending out beyond a radius of 100 km in Ex-I (Figure 9(i)).

Returning to early times, at 24 h the most prominent diabatic heating lies in an annulus located mostly outside the tangential wind-speed maximum, but weak inflow aloft extends across this band, due presumably in part to the diabatic heating at lesser radii. The effect of the inflow is manifest in the inward protruding 'noses' of the M surfaces, a feature that becomes more prominent with time (right panels of Figure 9). Some deep convection, as characterized by either the distribution of vertical motion or that of diabatic heating rate, becomes progressively focussed in a central region near the axis of rotation as the vortex intensifies.
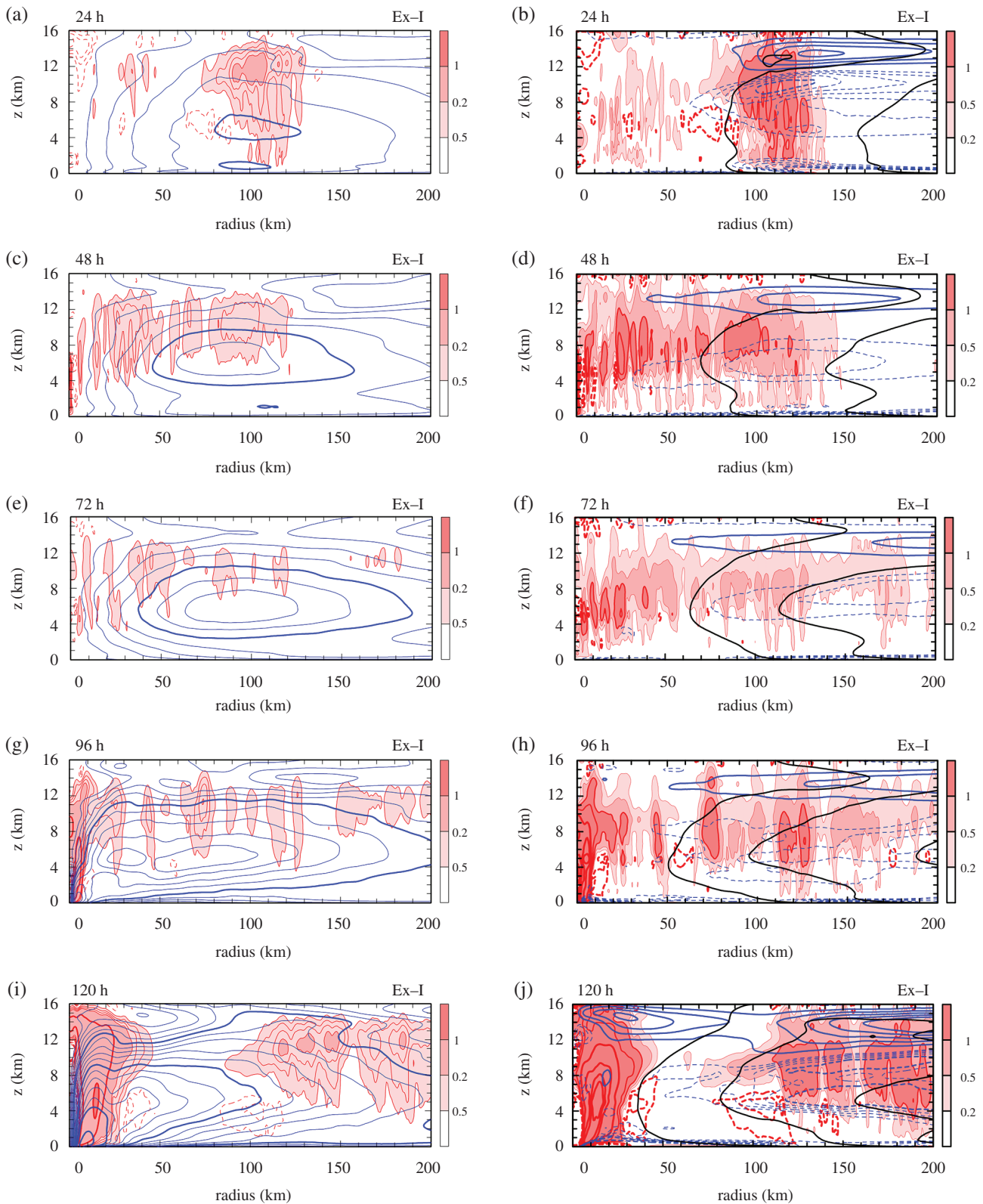
Figure 9. Vertical cross-sections of the azimuthally averaged, 3 h time-averaged tangential and radial velocity components centred at selected times in Ex-I. Superimposed (a, c, e, g, i) on the tangential component are contours of the averaged vertical velocity and (b, d, f, h, j) on the radial component the averaged diabatic heating rate, with shading as indicated, as well as selected contours of absolute angular momentum. Contour intervals are as follows. Tangential velocity: thin blue contours 1 m s^{-1} between 0 and 15 m s^{-1}, thick blue contours every 5 m s^{-1}. Vertical velocity: thin red contours every 0.05 to 2 m s^{-1}, thick red contour interval 0.5 m s^{-1}, thin dashed red contours indicate subsidence at intervals of 0.02 m s^{-1}. Radial velocity: thick blue positive contours 1 m s^{-1}, dashed negative, thin blue dashed contours every 0.2 m s^{-1} down to −0.8 m s^{-1}. Diabatic heating rate: thin red contours 0.2 and 0.5 K h^{-1}, dashed curves negative values, medium thickness red contours 1 and 2 K h^{-1}, thick red contours every 5 K h^{-1}. Shading as indicated on the side bar. Absolute angular momentum: thick black contours every 5 × 10^5 m^2 s^{-1}. [Colour figure can be viewed at wileyonlinelibrary.com].

This is, of course, a favourable location for convectively induced inflow to continually draw in the M surfaces, thereby intensifying the tangential wind, at least above the frictional boundary layer. The focusing, itself, must be aided by the strengthening boundary-layer inflow, which is evident in Figures 9(h) and (j).

At 96 h (Figure 9(g)), a second maximum in $\langle v(r, z)\rangle$ has begun to form near to the surface, inside a radius of 10 km, and by 120 h this maximum has grown in intensity to become the most prominent feature (Figure 9(i)), which explains why R_{max} decreases to less than 10 km (Figure 1(b)). Reasons for V_{max} to occur so close to the surface were anticipated long ago by
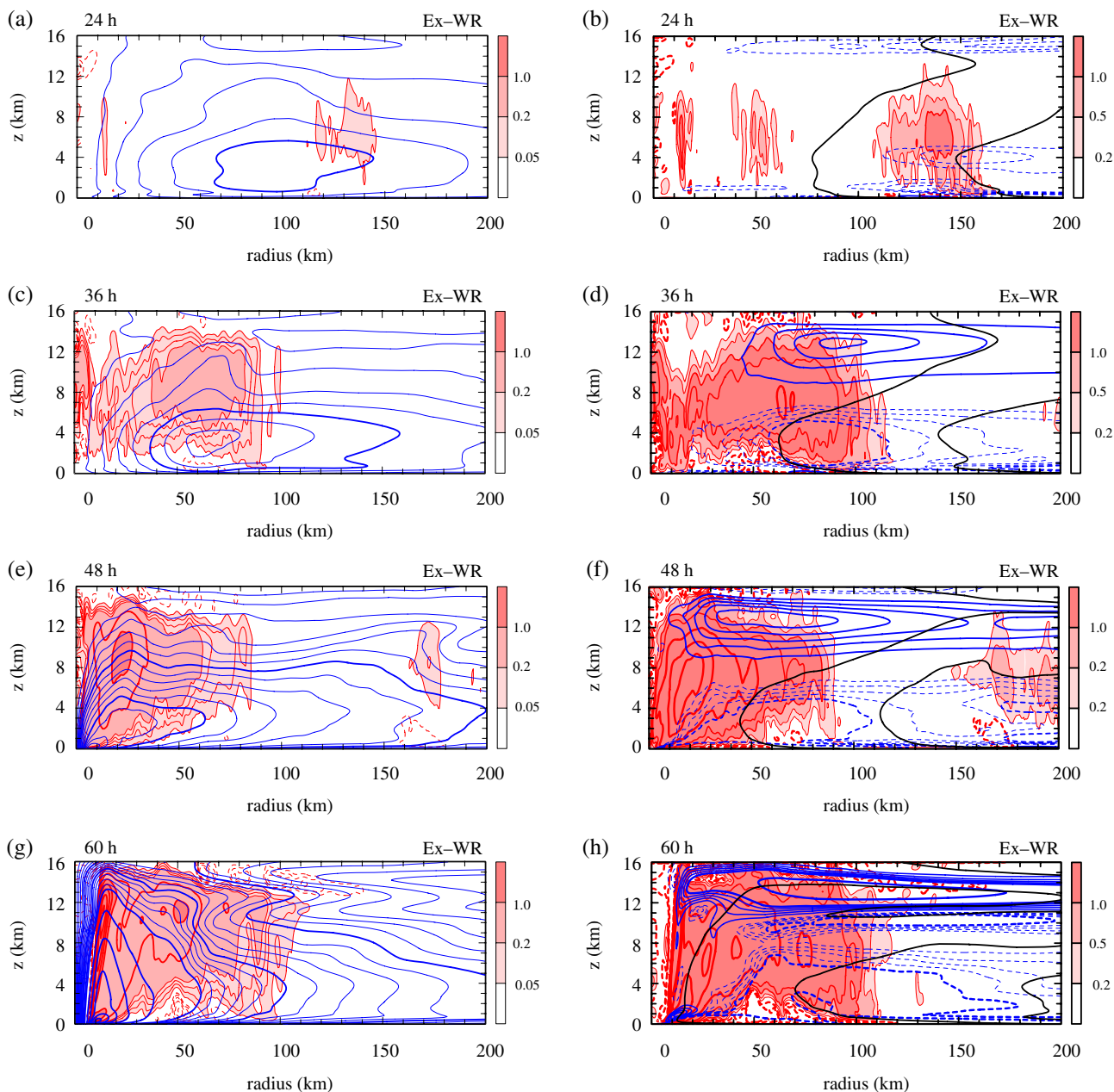
Figure 10. Legend as for Figure 9, except for Ex-WR. [Colour figure can be viewed at wileyonlinelibrary.com].

Anthes (1971). The mechanism by which this spin-up occurs has become known as the boundary-layer spin-up mechanism. A concise articulation of the mechanism is given by Smith and Montgomery (2016b). Although V_{max} at 120 h is less than $25 \, m \, s^{-1}$, the vortex structure has the main features of a tropical cyclone, at least from an azimuthally averaged perspective. These include strong low-level inflow, a tangential wind field that decreases in strength with height, a strong annular core of ascent with the maximum updraught away from the axis of rotation and a strong outflow layer in the upper troposphere (Figures 9(i) and (j)). The strengthening near-surface inflow as the vortex develops is seen in Figures 9(f), (h) and (j).

The foregoing pattern of evolution is similar in many respects to that in the Ex-WR simulation, where the genesis process is much more rapid and the formation of a low-level concentrated vortex is not preceded by the development of a broad tangential wind maximum in the middle troposphere (the early tangential wind maximum seen in Figures 10(a) and (c) is generally located below a height of about 3 km).

We have already discussed the reasons for the delayed genesis in the Ex-I simulation and turn now to examine the reasons for the early formation of a mid-level vortex in the simulation with ice microphysics.

4.1. Mid-level vortex development with ice microphysics

The occurrence of a mid-level vortex in individual mesoscale convective systems has been attributed to the vertical structure of the diabatic heating rate that exists in the extensive stratiform regions of these systems (e.g. Chen and Frank, 1993; Rogers and Fritsch, 2001). In these regions, there is heating due to latent heat release by the condensation of water vapour and the progressive freezing of liquid water in the weakly ascending anvils, but cooling in mesoscale downdraughts due to sublimation, melting and evaporation beneath the anvils (see e.g. Houze, 2014, section 9.6.3). This configuration of upper-tropospheric heating and lower-tropospheric cooling leads to a maximum vertical gradient of heating rate in the middle troposphere, rather than in the lower troposphere, associated with vigorous deep convective updraughts. Because the heating rate is approximately proportional to the vertical velocity, this pattern of heating rate is conducive through mass continuity to producing horizontal convergence in the middle troposphere rather than the lower troposphere. Near the freezing level, the convergence may be reinforced by the divergent stress generated by the melting of snow crystals just below the freezing level (typically 5.5 km in the Tropics). Since raindrops have fall speeds many times greater than

snowflakes, they exert a much larger collective drag on air below the freezing level than snowflakes exert above the freezing level. The vertical stress divergence leads to a horizontal convergence of the flow near the freezing level. In either case, the convergence will lead to an amplification of any existing vortical circulation (Haynes and McIntyre, 1987).

It seems plausible that the foregoing processes could account for the formation of the mid-level vortex seen in the Ex-I simulation. Moreover, since the mid-level inflow in this simulation is not just confined to the vicinity of the freezing level, the effect of the vertical gradient of the diabatic heating rate may be the dominant one for generating mid-level inflow and thereby for spinning up a mid-level cyclonic vortex. To explore this idea, we show in Figure 11 the inflow accompanying the balanced response of the time-averaged and azimuthally averaged tangential wind field $\langle v(r,z) \rangle$ to the time-averaged and azimuthally averaged diabatic heating rate $\langle \dot{\theta}(r,z) \rangle$ at selected times in the Ex-I and Ex-WR simulations. The balance calculations are carried out using the same methodology as in Smith *et al.* (2015b). In brief, $\langle \dot{\theta}(r,z) \rangle$ and $\langle v(r,z) \rangle$ are diagnosed from the corresponding output of the two simulations and then averaged over three-hour time periods to account in some way for the stochastic nature of deep convection in the two experiments. The balanced thermodynamic fields are then obtained from the spatial distribution of $\langle v(r,z) \rangle$ and the thermodynamic sounding at some large radius (here 500 km) using the method described by Smith (2006). Finally, the Sawyer–Eliassen equation is solved for the streamfunction of the secondary circulation using an open boundary condition at large radius (in this case 500 km).

The Sawyer–Eliassen equation, which has the same form as eq. (14) of Bui *et al.* (2009), is forced solely by the time average of $\langle \dot{\theta}(r,z) \rangle$ in an effort to isolate the effects of the diabatic heating alone on the distribution of inflow.¶ The solution method uses successive over-relaxation and is described in detail by Bui *et al.* (2009). In the present calculations,‖ the resolution of $\langle v(r,z) \rangle$ and $\langle \dot{\theta}(r,z) \rangle$ was degraded in the radial direction to facilitate convergence of the relaxation method in a reasonable time.

Comparison of the top four panels in Figure 11 with the corresponding panels in the right column of Figure 9 shows that, despite the degraded resolution,** the balance theory has considerable skill in capturing the time-averaged and azimuthally averaged radial flow obtained directly from the Ex-I simulation above the boundary layer.†† In particular, the balance solution is seen to capture the mid-tropospheric inflow well. For example, beyond 24 h the most prominent inflow forced by $\langle \dot{\theta}(r,z) \rangle$ in the Ex-I simulation occurs in a layer between 4 and 9 km. These results corroborate the findings of Montgomery *et al.* (2006), who demonstrated also the ability of balance solutions to capture the elevated inflow well in their vortex simulation with ice.

Comparison of the two bottom panels in Figure 11 with the corresponding panels in the right column of Figure 10 shows a similarly good agreement for the radial flow in

the lower troposphere above the boundary layer between the balanced calculation and the full solution in the Ex-WR simulation. In this case, the strongest inflow occurs below a height of 4 km.

The balance solutions provide strong support for the interpretation that the occurrence of the mid-level vortex in the Ex-I simulation is primarily a result of the more elevated vertical distribution of diabatic heating in this simulation, which is produced by the additional release of latent heat of freezing in the upper troposphere and the additional diabatic cooling just below the freezing level that accompanies melting.

From a vorticity perspective, the enhanced low-level vorticity near the circulation centre can come about only by a horizontal flux consisting of an advective and a non-advective component (Haynes and McIntyre, 1987). From this perspective, genesis is fundamentally a process involving the layerwise concentration of vertical vorticity. It then follows that there can be no net downward transport of vorticity from the middle-level vortex, ruling out the possibility of genesis being a 'top-down' process (Raymond *et al.*, 2011). In essence, any system-scale subsidence required to advect the mid-level vortex down would be accompanied by low-level radial outflow, which would dilute the vertical vorticity within any fixed circle. Equivalently, from an angular momentum perspective, the low-level radial outflow would move the M surfaces outwards, leading to a local spin-down of the tangential wind. In any case, as shown later in section 5, subsidence does not occur on the scale of either the mid-level vortex or the low-level vortex in Ex-I or Ex-WR within 24 h prior to genesis.

The rapid organization of the low-level vorticity between 80 and 90 h seen in Figure 8 strongly resembles that occurring prior to genesis in the Ex-WR simulation (see KSM, figure 3), suggesting the non-essential dynamical influence of the mid-level vortex.

4.2. Emerging boundary-layer control

The vertical cross-sections in Figure 9 show that, rather than the mid-tropospheric tangential wind maximum moving downwards, the tropical-cyclone vortex develops *in situ* by processes similar to those in the warm-rain-only simulation. In essence, the strengthening boundary-layer inflow seen in Figures 9(f), (h) and (j) is accompanied by a focusing and strengthening of the distribution of diabatic heating rate within a radius of less than 30 km and a progressive inward displacement of the M-surfaces, at least above the shallow boundary layer. The inward displacement of the averaged M-surfaces at low levels seen in the right panels of Figure 9 leads to a marked spin-up of the tangential wind field at low levels, as seen between panels (e), (g) and (i) of Figure 9. The fact that the maximum tangential wind speed at 120 h lies within the relatively strong inflow layer indicates that the boundary-layer spin-up mechanism referred to above has begun to operate.‡‡ The dynamics of formation of the low-level vortex broadly corroborate the results of earlier studies of the genesis problem by Montgomery *et al.* (2006), Nolan (2007) and Nicholls and Montgomery (2013).

5. A system-averaged view of vortex evolution

For completeness and to provide a comparison with the results in KSM, we examine briefly a system-averaged view of the genesis process in Ex-I. Figure 12 shows time–height cross-sections of system-averaged quantities within a column with horizontal cross-section 100 km × 100 km, centred at the centre of the circulation. These include the deviations of temperature and θ_e from their respective values at the start of the time series, the relative humidity (with respect to liquid water) and the vertical

---

¶It is important to note that, despite statements in the literature to the contrary by Stern *et al.* (2015), the forcing of the secondary circulation by radial and vertical gradients of diabatic heating cannot be completely isolated from forcing by boundary-layer friction, because the boundary layer in the inner-core region is intrinsically nonlinear (see e.g. Vogl and Smith, 2009; Smith and Montgomery, 2015; Montgomery and Smith 2017b). Nevertheless, friction by itself would generate radial outflow above the boundary layer: only diabatic heating can induce inflow both within and above the boundary layer and only then at radii outside the heating.

‖It may be worth pointing out that, during the very early phase of system scale vortex development, while the vortex is relatively weak, almost no regularization of the Sawyer–Eliassen equation is needed, because only a handful of points violate the ellipticity condition that guarantees a convergent balanced solution.

**Note that the degradation reduces the radial gradient of $\langle \dot{\theta}(r,z) \rangle$, which, by itself, would account for the weaker values of inflow in the balance calculations above the boundary layer. However, the smoothing leads to a more coherent forcing, which would tend to have the opposite effect.

††Of course, one cannot expect good agreement in the boundary layer (approximately the lowest km), as the flow there is typically not close to balance.

---

‡‡There is some indication of the boundary-layer spin-up process playing a slight role as early as 24 h to produce a weak maximum in the low-level tangential wind speed near a radius of 100 km in Figure 9(a).

Ice microphysics
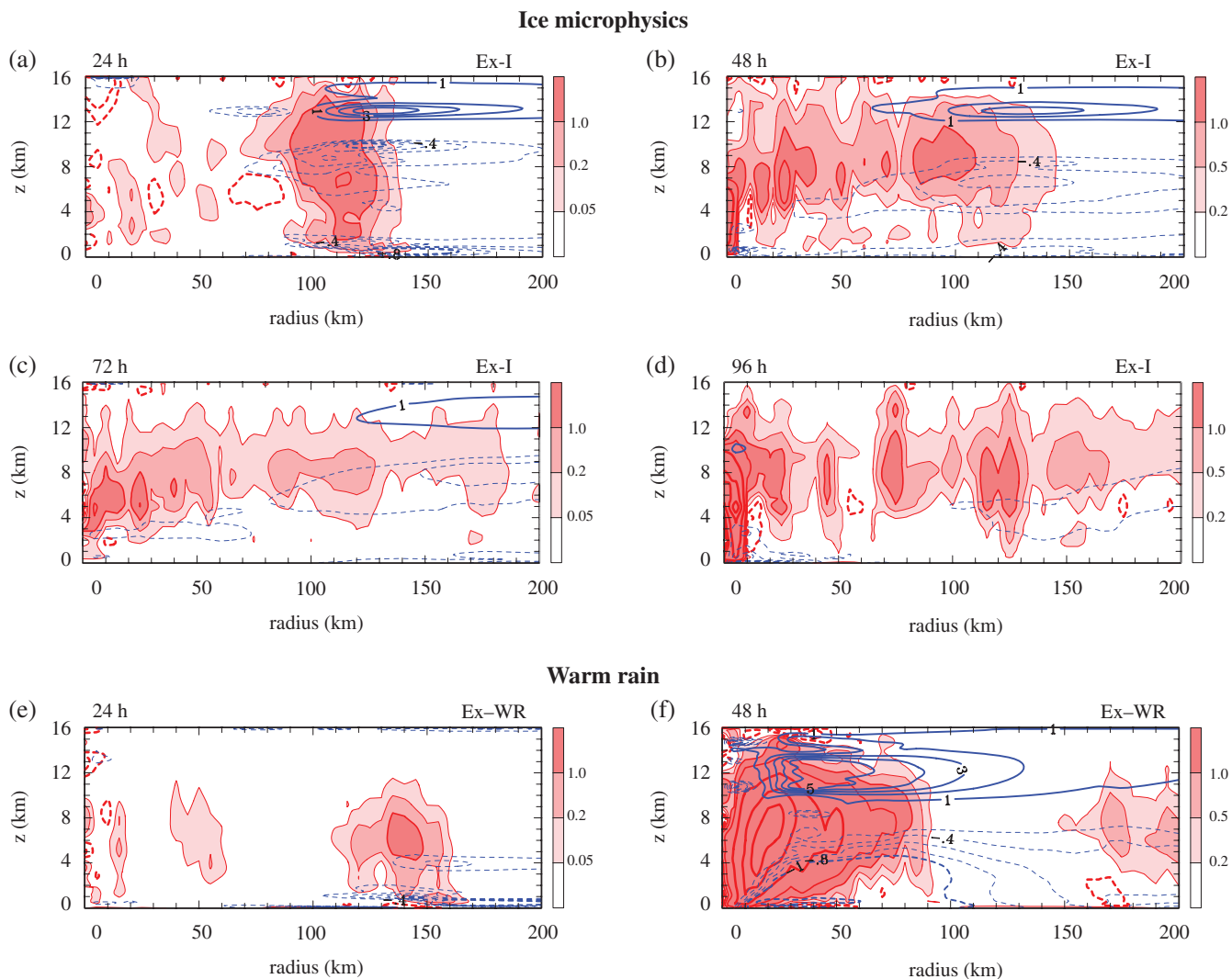
Figure 11. Radius–height cross-sections similar to the right panels of Figures 9 and 10, but showing the filtered diabatic heating rate and the balanced radial flow calculated from the solution of the Sawyer–Eliassen equation forced by this heating distribution. Contours of absolute angular momentum are not shown again. Contour information as in the caption to Figure 9. [Colour figure can be viewed at wileyonlinelibrary.com].
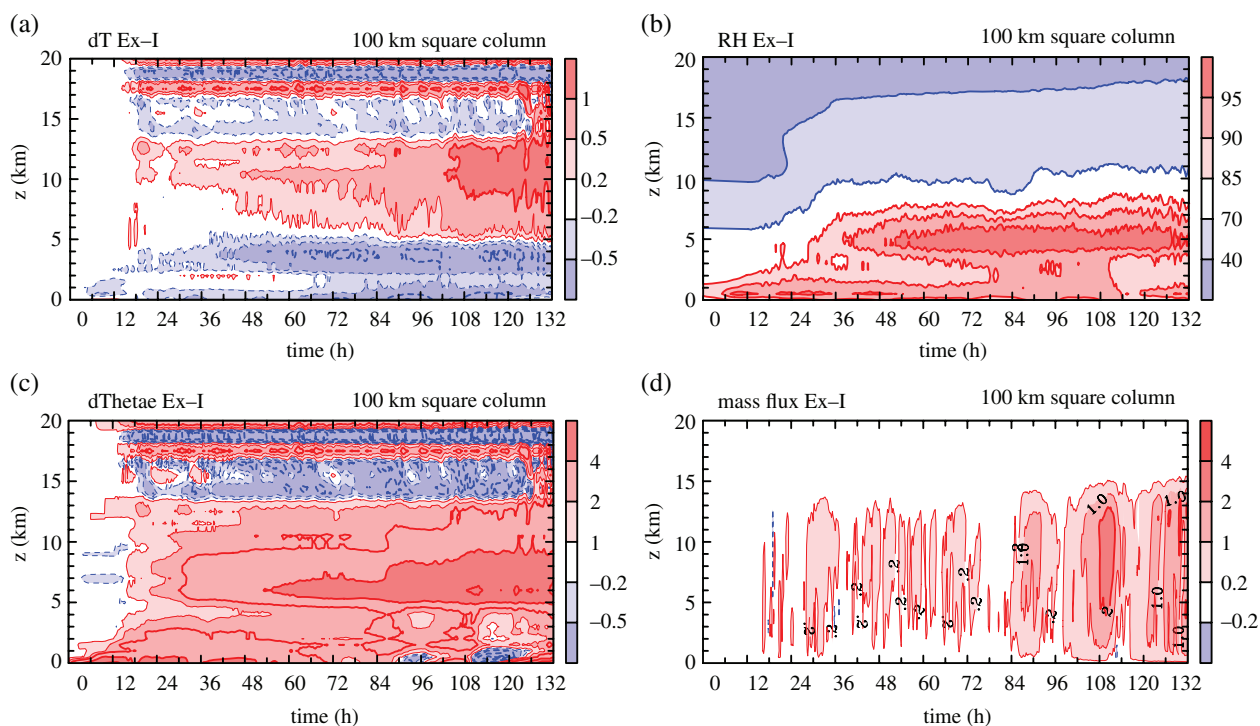
Figure 12. Time–height cross-sections of system-averaged quantities within a 100 km × 100 km column for Ex-I, centred on the circulation centre. These include (a) the temperature deviation from that at the start of the time series (K), (b) the relative humidity (per cent), (c) the equivalent potential temperature deviation from that at the start of the time series (K) and (d) the vertical mass flux per unit area (kg m^{-2} s^{-1}).
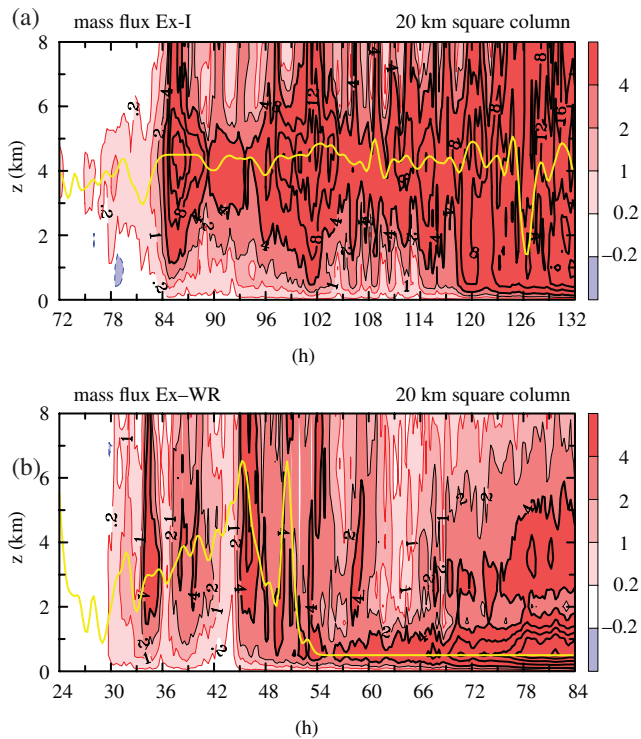
Figure 13. Time−height cross-sections of system-averaged mass flux within a 20 km × 20 km column centred on the circulation centre from (a) 72−132 h in Ex-I and (b) 24−84 h in Ex-WR. Values for the shading of mass flux are given in the colour bar, in units of kg m^{-2} s^{-1} multiplied by 10 for plotting purposes. The thin black contour is 2 kg m^{-2} s^{-1}; thick black contours for values every 4 kg m^{-2} s^{-1} from 4 kg m^{-2} s^{-1}. The yellow contour shows the height of the mass-flux maximum. Solid contours are positive, dashed contours negative. [Colour figure can be viewed at wileyonlinelibrary.com].

mass flux. Analogous cross-sections for the Ex-WR simulation are shown in figure 8 of KSM.

As in the Ex-WR simulation, the mid-to-upper troposphere warms while the lower troposphere cools (Figure 12(a)), but there is a large difference in the depth of significant cooling between both experiments. In Ex-I there is marked cooling (greater than 0.5 K difference) below a height of 5 km at most times, whereas in Ex-WR significant cooling is found only in the lowest 1.5 km (figure 8(a) of KSM). There is a clear humidification of the middle troposphere seen in both the relative humidity and perturbation θ_e cross-sections well prior to genesis (Figures 12(b) and (c)). The low to mid levels are drier than in Ex-WR, especially in the height range of 2−5 km. In particular, there are few occurrences below 4 km height where the relative humidity is greater than 95%. These differences are reflected in the θ_e fields also.

It is problematic to compare the relative humidity fields in the Ex-I and Ex-WR simulations above the freezing level, because the relative humidity is calculated in both cases with respect to liquid water. For this reason, values of relative humidity in the upper troposphere in Figure 12(b) are comparatively low. The humidification of the mid-troposphere found here prior to genesis corroborates the findings of Montgomery *et al.* (2006), Nolan (2007), Wang (2012) and references cited therein. In particular, Wang (2012) described the evolution of the pouch centre in her simulation as 'characterized by high saturation fraction, small difference in θ_e between the surface and the middle troposphere, and a short incubation time scale'.

The average net mass flux in the 100 km × 100 km column shows a degree of high-frequency variability to about 80 h. After this time, the variability diminishes and the magnitude increases, most notably after 120 h (Figure 12(d)). In this column, there is no systematic lowering of the height of maximum mass flux with time as hypothesized by Raymond *et al.* (2011, 2014) and discussed in the Introduction. Nevertheless, such a lowering is seen in a 20 km × 20 km column at later times (Figure 13(a)). Figure 13 shows similar time−height cross-sections of vertical

mass flux to Figure 4, but from 72−132 h in Ex-I and from 24−84 h in Ex-WR. Also shown is a yellow contour highlighting the height of the maximum mass flux. This narrower column is more representative of the scale of the low-level vortex.

In Ex-I, there is a systematic increase in the low-level mass flux from 84−132 h, although the maximum value remains mostly above a height of 4 km. In Ex-WR, the mass-flux maximum lowers to a height of about 500 m during the rapid intensification phase. The fact that there is a lowering of the height of maximum mass flux with time in Ex-WR, the simulation with no mid-level vortex, suggests that the mid-level vortex does not play an important role in this process. This finding removes a potential deficiency of the marsupial paradigm of Dunkerton *et al.* (2009) by not taking into account the role of a mid-level vortex (see the Introduction).

6. Sensitivity experiments

Figure 14 shows the evolution of V_{max} and $R_{v\,max}$ in Ex-I and the two moisture-perturbed runs. As in KSM, the inclusion of moisture perturbations in Experiments P1 and P2 leads to small differences in the onset of the intensification begin time. In P1 the intensification begin time occurs sooner than in the control (Ex-I) at about 90 h, whereas in P2 the intensification begin time occurs a few hours later than in Ex-I. The period of spin-down at about 105 h in Ex-I does not occur in either perturbed simulation. All three experiments have a similar $R_{v\,max}$ by the end of the calculations (132 h).

Due to the stochastic nature of deep convection, differences in the details of vortex evolution in the perturbed simulations are to be expected (e.g. Nguyen *et al.*, 2008; Shin and Smith, 2008). As in the case without ice, a comparison of horizontal cross-sections of vertical velocity and vertical vorticity in Ex-1, P1 and P2 provides evidence of this stochastic nature (not shown). There are significant differences in the detailed patterns of deep convection and relative vorticity fields in the three experiments. Despite these differences, the intensification begin time in all three experiments is relatively close, supporting the robustness of the results presented herein.

As suggested in KSM, this lack of sensitivity might be due to the addition of moisture perturbations on the fine grid scale being used, rather than larger scale perturbations (Weckwerth, 2000; Shin and Smith, 2008). A more complete examination of the dependence of the solution on the scale of moisture perturbations is a topic that warrants future study.

7. Some remaining issues

We examine now briefly the proposal of Wang (2014) that tropical cyclone formation can be regarded as a two-stage process. She describes the first stage as a gradual process of moisture preconditioning and low-level spin-up, in which 'cumulus congestus plays a dominant role in moistening the lower to middle troposphere and spinning up the near-surface circulation prior to genesis, while deep convection plays a key role in moistening the upper troposphere and intensifying the cyclonic circulation over a deep layer'.

While we would agree that cumulus congestus would contribute to the genesis process in the way that Wang describes, if it were the *dominant process* then one would expect to see a prominent outflow region in the middle troposphere associated with this convection. In the results we have presented, we do not find such mid-tropospheric outflow in either the EX-WR or EX-I simulations. Rather, the system-scale outflow in these experiments is found in the upper troposphere, reflecting the dominance of deep convection.

Wang's second stage of formation 'commences with the rapid development of deep convection in the inner pouch region after the air column is moistened sufficiently, whereupon the concentrated convective heating near the pouch center

(a)

(b)
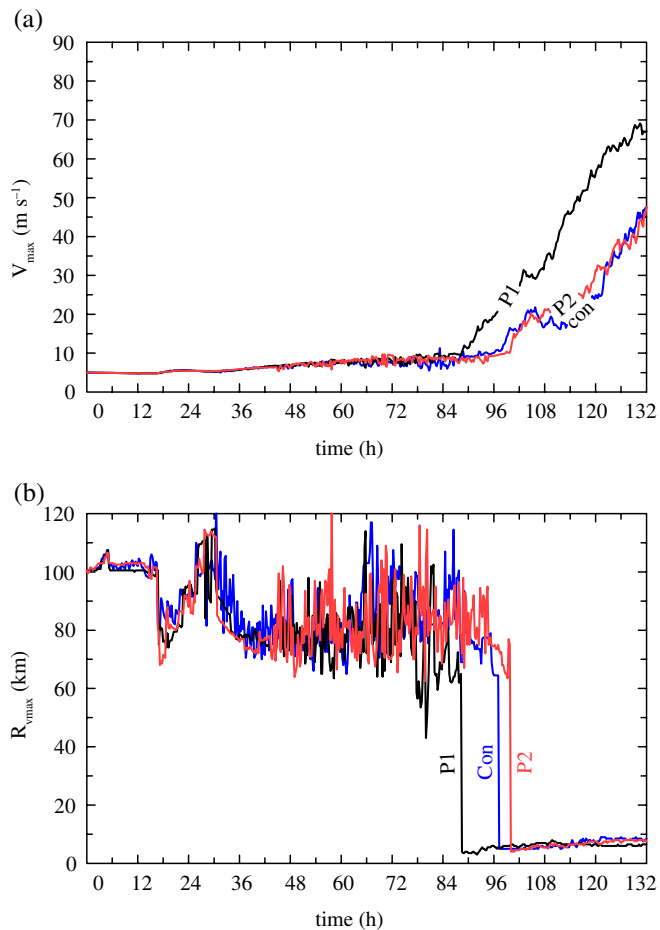
Figure 14. Time series of (a) maximum azimuthally averaged tangential wind speed (V_{max}) and (b) the radius $R_{v\,max}$ at which the maximum tangential wind speed occurs in the control experiment (Ex-I, blue curve labelled 'con') and two experiments similar to the control, but with perturbations to the initial boundary-layer moisture (black and red curves, labelled 'P1' and 'P2', respectively). [Colour figure can be viewed at wileyonlinelibrary.com].

strengthens the transverse circulation and leads to the amplification of the cyclonic circulation over a deep layer'. She invokes 'the power-law increase of precipitation rate with column water vapor (CWV) above a critical value' to explain 'the rapid development of deep convection', arguing further that 'the high CWV near the pouch center thus plays an important role in convective organization'. Our results presented above suggest an alternative explanation for the development of deep convection, namely the steady strengthening of boundary-layer inflow (and implied convergence) and the progressive control on deep convection exerted by the boundary layer, both dynamic and thermodynamic, as articulated by Persing *et al.* (2013, see p. 12334) and Kilroy *et al.* (2016b). A thorough examination of Wang's proposed second phase of development is beyond the scope of the current study and will be a topic of future investigation.

8. Conclusions

We have extended a recent idealized numerical study of tropical cyclogenesis to investigate the additional effects of incorporating ice. When ice processes are included, the gestation time before genesis occurs is more than twice as long as in the warm-rain-only simulation. Moreover, this gestation period is characterized by the formation of a moderate strength system-scale vortex in the middle troposphere. Reasons for the longer gestation period in the case with ice were offered.

Axisymmetric balance calculations showed that the spin-up of the mid-level vortex is related to the larger horizontal and vertical gradient of diabatic heating rate in the middle troposphere

than in the warm-rain-only simulation. The elevated gradient of heating rate leads to a *system-scale* radial influx of absolute vorticity in the middle troposphere, or equivalently, from an azimuthally averaged perspective, to an inward displacement of absolute angular momentum surfaces at these altitudes. In either perspective, the inflow leads to a spin-up of the tangential wind at middle levels.

The formation of the tropical-cyclone vortex in the simulation with ice is similar to that in the warm-rain-only simulation, with the strengthening frictional boundary layer exerting a progressively important role in focusing inner-core deep convection. This vortex develops *in situ* on a much smaller scale than the mid-level vortex by processes that are similar to those in the warm-rain-only simulation, in which no such mid-level vortex forms. Indeed, there is no evidence that the low-level vortex forms as a result of the mid-level vortex being somehow carried downwards.

We pointed out that, from a vorticity perspective, the enhanced low-level vorticity near the circulation centre can come about only by a horizontal flux consisting of an advective and a non-advective component. Accordingly, there can be no net downward transport of vorticity from the middle-level vortex, ruling out the possibility of genesis being a 'top-down' process.

The rapid organization of the low-level vorticity in the ice experiment strongly resembles that occurring prior to genesis in the warm-rain-only simulation, suggesting the non-essential dynamical influence of the mid-level vortex. The fact that genesis occurs in a similar way in the five warm-rain simulations, which do not have a mid-level vortex, suggests to us that the mid-level vortex does not play an essential thermodynamical role either. The height of the maximum mass flux in the ice simulation is not systematically lowered prior to the rapid spin-up of the low-level circulation. If found to be general, this result would have implications for the Raymond theory, which invokes the lowering of the mass flux in association with the development of a middle-level cyclonic vortex.

Taken together, the results for the warm-rain-only and ice simulations suggest that the formation of the mid-level vortex is not a prerequisite for explaining tropical cyclogenesis in a favourable, moist, pouch-like environment with minimal vertical shear.

References

Anthes RA. 1971. Iterative solutions to the steady-state axisymmetric boundary-layer equations under an intense pressure gradient. *Mon. Weather Rev.* **99**: 261–268.

Barnes GM, Zipser EJ, Jorgensen D, Marks F. 1983. Mesoscale and convective structure of a hurricane rainband. *J. Atmos. Sci.* **40**: 2125–2137.

Bister M, Emanuel KA. 1998. Dissipative heating and hurricane intensity. *Meteorol. Atmos. Phys.* **65**: 233–240.

Bryan GH, Fritsch JM. 2002. A benchmark simulation for moist non-hydrostatic numerical models. *Mon. Weather Rev.* **130**: 2917–2928.

Bui HH, Smith RK, Montgomery MT, Peng J. 2009. Balanced and unbalanced aspects of tropical-cyclone intensification. *Q. J. R. Meteorol. Soc.* **135**: 1715–1731.

Callaghan J, Smith RK. 1998. The relationship between maximum surface wind speeds and central pressure in tropical cyclones. *Aust. Meteorol. Mag.* **47**: 191–202.

Chen SS, Frank WM. 1993. A numerical study of the genesis of extratropical convective mesovortices. Part I: Evolution and dynamics. *J. Atmos. Sci.* **50**: 2401–2426.

Dunkerton TJ, Montgomery MT, Wang Z. 2009. Tropical cyclogenesis in a tropical wave critical layer: Easterly waves. *Atmos. Chem. Phys.* **9**: 5587–5646.

Emanuel KA. 1989. The finite amplitude nature of tropical cyclogenesis. *J. Atmos. Sci.* **46**: 3431–3456.

Frank WM. 1987. Tropical cyclone formation. In *A Global View of Tropical Cyclones*, Elsberry RL. (ed.): 53–90. Office of Naval Research: Arlington, VA.

Haynes P, McIntyre ME. 1987. On the evolution of vorticity and potential vorticity in the presence of diabatic heating and frictional or other forces. *J. Atmos. Sci.* **44**: 828–841.

Houze RA. 2004. Mesoscale convective systems. *Rev. Geophys.* **42**: RG4003. https://doi.org/10.1029/2004RG000150.

Houze RA. 2014. *Cloud Dynamics*, *International Geophysics Series* **104**: Oxford, UK.

Karyampudi VM, Pierce HF. 2002. Synoptic-scale influence of the Saharan air layer on tropical cyclogenesis over the eastern Atlantic. *Mon. Weather Rev.* **130**: 3100–3128.

Kilroy G, Smith RK. 2017. The effects of initial vortex size on hurricane genesis and intensification. *Q. J. R. Meteorol. Soc.* **143**: 2832–2845.

Kilroy G, Smith RK, Wissmeier U. 2014. Tropical convection: The effects of ambient vertical and horizontal vorticity. *Q. J. R. Meteorol. Soc.* **140**: 1756–1770.

Kilroy G, Smith RK, Montgomery MT, Lynch B, Earl-Spurr C. 2016a. A case study of a monsoon low that formed over the sea and intensified over land as seen in the ECMWF analyses. *Q. J. R. Meteorol. Soc.* **142**: 2244–2255.

Kilroy G, Smith RK, Montgomery MT. 2016b. Why do model tropical cyclones grow progressively in size and decay in intensity after reaching maturity? *J. Atmos. Sci.* **73**: 487–503.

Kilroy G, Smith RK, Montgomery MT. 2017. A unified view of tropical cyclogenesis and intensification. *Q. J. R. Meteorol. Soc.* **143**: 450–462.

Lajoie F, Walsh K. 2008. A technique to determine the radius of maximum wind of a tropical cyclone. *Weather and Forecasting* **23**: 1007–1015.

Lord SJ, Willoughby HE, Piotrowicz JM. 1984. Role of a parameterized ice-phase microphysics in an axisymmetric, non-hydrostatic tropical cyclone model. *J. Atmos. Sci.* **41**: 2836–2848.

McBride JL. 1995. Tropical cyclone formation. In *Global Perspectives on Tropical Cyclones*, WMO/TD-No 693, Elsberry RL. (ed.): pp. 21–62. World Meteorological Organization: Geneva, Switzerland.

McCumber M, Tao W, Simpson J, Penc R, Soong S. 1991. Comparison of ice-phase microphysical parameterization schemes using numerical simulations of tropical convection. *J. Appl. Meteorol.* **30**: 985–1004.

Montgomery MT, Smith RK. 2011. 'Tropical-cyclone formation: Theory and idealized modelling'. In *Proceedings of Seventh WMO International Workshop on Tropical Cyclones (IWTC–VII)*, LaRéunion, France, November 2010. World Meteorological Organization: Geneva, Switzerland (WWRP 2011-1).

Montgomery MT, Smith RK. 2014. Paradigms for tropical-cyclone intensification. *Aust. Meteorol. Oceanogr. J.* **64**: 37–66.

Montgomery MT, Smith RK. 2017a. Recent developments in the fluid dynamics of tropical cyclones. *Annu. Rev. Fluid Mech.* **49**: 1–33.

Montgomery MT, Smith RK. 2017b. On the applicability of linear, axisymmetric dynamics in intensifying and mature tropical cyclones. *Flluids*, (in press). doi:10.3390/flluids2040069.

Montgomery MT, Nicholls ME, Cram TA, Saunders A. 2006. A 'vortical' hot tower route to tropical cyclogenesis. *J. Atmos. Sci.* **63**: 355–386.

Montgomery MT, Lussier LL, Moore RW, Wang ZW. 2010. The genesis of Typhoon Nuri as observed during the Tropical Cyclone Structure 2008 (TCS-08) field experiment. Part 1: The role of the easterly wave critical layer. *Atmos. Chem. Phys.* **10**: 9879–9900.

Morrison H, Curry JA, Khvorostyanov VI. 2005. A new double-moment microphysics parameterization for application in cloud and climate models. Part I: Description. *J. Atmos. Sci.* **62**: 1665–1677.

Nguyen SV, Smith RK, Montgomery MT. 2008. Tropical-cyclone intensification and predictability in three dimensions. *Q. J. R. Meteorol. Soc.* **134**: 563–582.

Nicholls M, Montgomery MT. 2013. An examination of two pathways to tropical cyclogenesis occurring in idealized simulations with a cloud-resolving numerical model. *Atmos. Chem. Phys.* **13**: 5999–6022.

Nolan DS. 2007. What is the trigger for tropical cyclogenesis? *Aust. Meteorol. Mag.* **56**: 241–266.

Penny AB, Harr PA, Doyle JD. 2016. Sensitivity to the representation of microphysical processes in numerical simulations during tropical storm formation. *Mon. Weather Rev.* **144**: 3611–3630.

Persing J, Montgomery MT, McWilliams J, Smith RK. 2013. Asymmetric and axisymmetric dynamics of tropical cyclones. *Atmos. Chem. Phys.* **13**: 12249–12341.

Raymond DJ, López-Carillo C. 2011. The vorticity budget of developing Typhoon Nuri (2008). *Atmos. Chem. Phys.* **11**: 147–163.

Raymond DJ, Sessions SL. 2007. Evolution of convection during tropical cyclogenesis. *Geophys. Res. Lett.* **34**: L06811. https://doi.org/10.1029/2006GL028607.

Raymond DJ, Sessions SL, López Carrillo C. 2011. Thermodynamics of tropical cyclogenesis in the northwest Pacific. *J. Geophys. Res.* **116**: D18101. https://doi.org/10.1029/2011JD015624.

Raymond DJ, Gjorgjievska S, Sessions S, Fuchs Z. 2014. Tropical cyclogenesis and mid-level vorticity. *Aust. Meteorol. Oceanogr. J.* **64**: 11–25.

Rogers RF, Fritsch JM. 2001. Surface cyclogenesis from convectively driven amplification of midlevel mesoscale convective vortices. *Mon. Weather Rev.* **129**: 605–637.

Shin S, Smith RK. 2008. Tropical-cyclone intensification and predictability in a minimal three-dimensional model. *Q. J. R. Meteorol. Soc.* **134**: 1661–1671.

Simpson J, Ritchie E, Holland GJ, Halverson J, Stewart S. 1997. Mesoscale interactions in tropical cyclone genesis. *Mon. Weather Rev.* **125**: 2643–2661.

Smith RK. 2006. Accurate determination of a balanced axisymmetric vortex. *Tellus* **58A**: 98–103.

Smith RK, Montgomery MT. 2012. Observations of the convective environment in developing and non-developing tropical disturbances. *Q. J. R. Meteorol. Soc.* **138**: 1721–1739.

Smith RK, Montgomery MT. 2015. Towards clarity on understanding tropical cyclone intensification. *J. Atmos. Sci.* **72**: 3020–3031.

Smith RK, Montgomery MT. 2016a. The efficiency of diabatic heating and tropical cyclone intensification. *Q. J. R. Meteorol. Soc.* **142**: 2081–2086.

Smith RK, Montgomery MT. 2016b. Comments on: 'Nonlinear response of a tropical cyclone vortex to prescribed eyewall heating with and without surface friction in TCM4: Implications for tropical cyclone intensification', by J. Heng and Y. Wang. *J. Atmos. Sci.* **73**: 5101–5103.

Smith RK, Montgomery MT, Kilroy G, Tang S, Müller SK. 2015a. Tropical low formation during the Australian monsoon: The events of January 2013. *Aust. Meteorol. Oceanogr. J.* **65**: 318–341.

Smith RK, Kilroy G, Montgomery MT. 2015b. Why do model tropical cyclones intensify more rapidly at low latitudes? *J. Atmos. Sci.* **72**: 1783–1804.

Srivastava RC. 1987. A model of intense downdrafts driven by the melting and evaporation of precipitation. *J. Atmos. Sci.* **44**: 1752–1774.

Stern DP, Vigh JL, Nolan DS, Zhang F. 2015. Revisiting the relationship between eyewall contraction and intensification. *J. Atmos. Sci.* **72**: 1283–1306.

Tang S, Smith RK, Montgomery MT, Gu M. 2016. Numerical study of the spin up of a tropical low over land during the Australian monsoon. *Q. J. R. Meteorol. Soc.* **142**: 2021–2032.

Tory K, Frank WM. 2010. Tropical cyclone formation. In *Chapter 2 of Global Perspectives on Tropical Cyclones: From Science to Mitigation*, Series on AsiaPacific Weather and Climate 4, Kepert JD, Chan JCL. (eds.). World Scientific: Singapore.

Vigh JL, Schubert WH. 2009. Rapid development of the tropical cyclone warm core. *J. Atmos. Sci.* **66**: 3335–3350.

Vogl S, Smith RK. 2009. Limitations of a linear model for the hurricane boundary layer. *Q. J. R. Meteorol. Soc.* **135**: 839–850.

Wang Y. 2002. An explicit simulation of tropical cyclones with a triply nested movable mesh primitive equation model: TCM3. Part II: Model refinements and sensitivity to cloud microphysics mararemization. *Mon. Weather Rev.* **130**: 3022–3036.

Wang Z. 2012. Thermodynamic aspects of tropical cyclone formation. *J. Atmos. Sci.* **69**: 2433–2451.

Wang Z. 2014. Role of cumulus congestus in tropical cyclone formation in a high-resolution numerical model simulation. *J. Atmos. Sci.* **71**: 1681–1700.

Wang Z, Montgomery MT, Dunkerton TJ. 2010. Genesis of Pre-hurricane Felix (2007). Part I: The role of the easterly wave critical layer. *J. Atmos. Sci.* **67**: 1711–1729.

Weckwerth TM. 2000. The effect of small-scale moisture variability on thunderstorm initiation. *Mon. Weather Rev.* **128**: 4017–4030.

Williams E, Renno N. 1993. An analysis of the conditional instability of the tropical atmosphere. *Mon. Weather Rev.* **121**: 21–36.

Willoughby HE, Jin H, Lord SJ, Piotrowicz JM. 1984. Hurricane structure and evolution as simulated by an axisymmetric, non-hydrostatic numerical model. *J. Atmos. Sci.* **41**: 1169–1186.

Zhu T, Zhang D. 2006. Numerical simulation of Hurricane *Bonnie* (1998). Part II: Sensitivity to varying cloud microphysical processes. *J. Atmos. Sci.* **63**: 109–126.

Zipser EJ. 2003. Some views on Hot Towers after 50 years of tropical field programs and two years of TRMM data. *Meteorol. Monogr.* **51**: 49–58.